The Astrophysical Journal, 1002:192 (23pp), 2026 May 10 https://doi.org/10.3847/1538-4357/ae5bac

Large-scale Structure in COSMOS-Web: Tracing Galaxy Evolution in the Cosmic Web up to $z \sim 7$ with the Largest JWST Survey

Hossein Hatamnia[1], Bahram Mobasher[1], Sina Taamoli[1], Jeyhan S. Kartaltepe[2], Caitlin M. Casey[3,4], Hollis B. Akins[5], Malte Brinch[6,7], Nima Chartab[8], Nicole E. Drakos[9], Andreas L. Faisst[8], Steven L. Finkelstein[5,10], Maximilien Franco[11], Finn Giddings[12], Ghassem Gozaliasl[13,14], Ali Hadi[1], Aryana Haghjoo[1], Santosh Harish[2], Olivier Ilbert[15], Pascale L. Jablonka[16], Shuowen Jin[4,17], Ali Ahmad Khostovan[2,18], Anton M. Koekemoer[19], Ronaldo Laishram[20], Daizhong Liu[21], Matteo Maturi[22,23], Henry Joy McCracken[24], Crystal L. Martin[3], Lauro Moscardini[25,26,27], Diana Scognamiglio[28], Marko Shuntov[4], Greta Toni[22,25,26], Alexander de la Vega[1], John R. Weaver[29,30], and Lilan Yang[2]

[1] Department of Physics and Astronomy, University of California, Riverside, 900 University Avenue, Riverside, CA 92521, USA; hossein.hatamnia@email.ucr.edu
[2] Laboratory for Multiwavelength Astrophysics, School of Physics and Astronomy, Rochester Institute of Technology, 84 Lomb Memorial Drive, Rochester, NY 14623, USA
[3] Department of Physics, University of California, Santa Barbara, Santa Barbara, CA 93106, USA
[4] Cosmic Dawn Center (DAWN), Denmark
[5] Department of Astronomy, The University of Texas at Austin, 2515 Speedway Blvd Stop C1400, Austin, TX 78712, USA
[6] Instituto de Física y Astronomía, Universidad de Valparaíso, Avda. Gran Bretanã 1111, Valparaíso, Chile
[7] Millennium Nucleus for Galaxies (MINGAL), Chile
[8] Caltech/IPAC, MS 314-6, 1200 E. California Blvd. Pasadena, CA 91125, USA
[9] Department of Physics and Astronomy, University of Hawaii, Hilo, 200 W Kawili St, Hilo, HI 96720, USA
[10] Cosmic Frontier Center, The University of Texas at Austin, Austin, TX 78712, USA
[11] Université Paris-Saclay, Université Paris Cité, CEA, CNRS, AIM, 91191, Gif-sur-Yvette, France
[12] Institute for Astronomy, University of Hawai'i, 2680 Woodlawn Drive, Honolulu, HI 96822, USA
[13] Department of Computer Science, Aalto University, P.O. Box 15400, FI-00076 Espoo, Finland
[14] Department of Physics, University of Helsinki, P.O. Box 64, FI-00014 Helsinki, Finland
[15] Aix Marseille Univ, CNRS, CNES, LAM, Marseille, France
[16] Ecole Polytechnique Fédérale de Lausanne, CH-1015 Lausanne, Switzerland
[17] DTU Space, Technical University of Denmark, Elektrovej 327, 2800 Kgs. Lyngby, Denmark
[18] Department of Physics and Astronomy, University of Kentucky, 505 Rose Street, Lexington, KY 40506, USA
[19] Space Telescope Science Institute, 3700 San Martin Drive, Baltimore, MD 21218, USA
[20] National Astronomical Observatory of Japan, 2-21-1 Osawa, Mitaka, Tokyo 181-8588, Japan
[21] Purple Mountain Observatory, Chinese Academy of Sciences, 10 Yuanhua Road, Nanjing 210023, People's Republic of China
[22] Zentrum für Astronomie, Universität Heidelberg, Philosophenweg 12, D-69120, Heidelberg, Germany
[23] Institute for Theoretical Physics, Philosophenweg 16, D-69120 Heidelberg, Germany
[24] Institut d'Astrophysique de Paris, UMR 7095, CNRS, and Sorbonne Université, 98 bis boulevard Arago, F-75014 Paris, France
[25] University of Bologna—Department of Physics and Astronomy "Augusto Righi" (DIFA), Via Gobetti 93/2, I-40129 Bologna, Italy
[26] INAF—Osservatorio di Astrofisica e Scienza dello Spazio, Via Gobetti 93/3, I-40129, Bologna, Italy
[27] INFN—Sezione di Bologna, Viale Berti Pichat 6/2, I-40127, Bologna, Italy
[28] Jet Propulsion Laboratory, California Institute of Technology, 4800 Oak Grove Drive, Pasadena, CA 91109, USA
[29] MIT Kavli Institute for Astrophysics and Space Research, 70 Vassar Street, Cambridge, MA 02139, USA
Received 2025 November 12; revised 2026 March 18; accepted 2026 April 4; published 2026 May 6

Abstract

We present a reconstruction of the large-scale structure, using the James Webb Space Telescope (JWST) COSMOS-Web program to trace environmentally driven galaxy evolution up to $z \sim 7$. We apply a weighted kernel density estimation method to 164,000 galaxies with robust photometric redshifts. We find that stellar mass has a positive correlation with density at all redshifts, which is stronger for quiescent galaxies (QGs) at $z \lesssim 2.5$, while at higher redshifts ($2.5 \lesssim z \lesssim 5.5$) this trend is confined to extreme overdense environments, consistent with early mass assembly in protoclusters. The star formation rate (SFR) shows a negative trend with density for QGs at $z \lesssim 1.2$, reversing at $z \gtrsim 1.8$, while star-forming galaxies (SFGs) show a mild positive correlation up to $z \sim 5.5$. The specific SFR remains nearly flat for SFGs and declines with density for QGs at $z \lesssim 1.2$. Moreover, mass and environmental quenching efficiencies show that mass-driven processes dominate at $z \gtrsim 2.5$, that the two processes act with comparable strength between $0.8 \lesssim z \lesssim 2.5$, and that environmental quenching becomes stronger for low-mass galaxies ($M_\star \lesssim 10^{10} M_\odot$) at $z \lesssim 0.8$. These findings reveal that large-scale structure drives galaxy evolution by enhancing early mass assembly in dense regions and increasingly suppressing star formation in low-mass systems at later times, establishing the environmental role of the cosmic web across cosmic history. COSMOS-Web, the largest JWST survey, provides accurate and deep photometric redshifts, reaching 80% mass completeness at

[30] Brinson Prize Fellow.

$\log M_\star/M_\odot \sim 8.7$ at $z \sim 7$, enabling the first view of how environments shaped galaxy evolution from the Epoch of Reionization to the present day.

Unified Astronomy Thesaurus concepts: Large-scale structure of the universe (902); Galaxy evolution (594); Star formation (1569); Quenched galaxies (2016)

Materials only available in the online version of record: figure set

1. Introduction

The large-scale structure (LSS) of the Universe consists of nodes, filaments, sheets, and voids, forming the cosmic web. These structures grew from small density fluctuations in the early Universe (Y. B. Zel'dovich 1970; J. R. Bond et al. 1996) and are reproduced in cosmological simulations such as the Millennium Simulation (V. Springel et al. 2005) and IllustrisTNG (D. Nelson et al. 2018), which also provide a framework for connecting the cosmic web to the formation and evolution of galaxies (M. L. Balogh 2004; G. Kauffmann et al. 2004; N. Chartab et al. 2025). Observable properties of galaxies—such as the stellar mass and star formation rate (SFR)—are known to be affected by their environment (Y.-j. Peng et al. 2010; N. Scoville et al. 2013; B. Darvish et al. 2016; N. Chartab et al. 2020; S. Taamoli et al. 2024a). Although many features of the large-scale distribution of matter are successfully predicted by the standard ΛCDM model of cosmology, several observational tensions remain, including the Hubble tension (see, e.g., E. Di Valentino et al. 2021 for a review) and the σ_8 tension (H. Hildebrandt et al. 2017; S. Joudaki et al. 2018). ΛCDM also faces challenges on smaller, highly nonlinear scales, including discrepancies in halo structure, galaxy clustering, and subhalo abundance (J. S. Bullock & M. Boylan-Kolchin 2017; L. Perivolaropoulos & F. Skara 2022; L. V. Sales et al. 2022; M. Khoshtinat et al. 2024). These challenges highlight the importance of studying the cosmic web to understand galaxy evolution and constrain cosmological parameters.

Early spectroscopic surveys—such as the Two Degree Field Galaxy Redshift Survey (M. Colless et al. 2003) and the Sloan Digital Sky Survey (D. G. York et al. 2000)—provided the first direct maps of the cosmic web on scales of hundreds of megaparsecs (A. Doroshkevich et al. 2004; M. Tegmark et al. 2004). Deep multiwavelength programs, including COSMOS (N. Scoville et al. 2007) and CANDELS (N. A. Grogin et al. 2011; A. M. Koekemoer et al. 2011), extended these measurements to progressively higher redshifts, enabling statistical studies of how galaxy properties depend on environment across cosmic time. Pushing such analyses beyond $z \sim 2$ revealed prominent overdense structures at early epochs, including large galaxy concentrations, such as the SSA22 field at $z \sim 3$ (C. C. Steidel et al. 1998), demonstrating that significant clustering was already established. Since then, numerous high-redshift protocluster candidates have been identified using different tracers, including narrowband-selected Lyα emitters, Lyman-break galaxies, and spectroscopic overdensities (C. M. Casey 2016; R. A. Overzier 2016; A. B. Newman et al. 2020). Although these efforts have advanced our understanding of early cluster assembly, they often rely on specific galaxy populations and limited survey volumes. As redshift increases, smaller sample sizes, larger photometric uncertainties, and the incomplete coverage of low-mass systems further complicate environmental reconstruction and can bias the identification and interpretation of overdensity peaks (D. C. Baxter et al. 2025).

Stellar mass and SFR are the most fundamental quantities for understanding galaxy growth and quenching, as they directly trace both the buildup of stellar populations and ongoing star formation activity. Stellar mass records the cumulative history of star formation and mergers (C. A. Tremonti et al. 2004; A. Gallazzi et al. 2005; L. J. Tacconi et al. 2020), correlates with morphology and quiescence (G. Kauffmann et al. 2003; Y.-j. Peng et al. 2010) and metallicity (C. A. Tremonti et al. 2004), and connects to structural parameters (such as size and mass density) and halo properties that regulate star formation (S. Shen et al. 2003; A. Dekel & Y. Birnboim 2006; B. P. Moster et al. 2010; P. S. Behroozi et al. 2013; A. van der Wel et al. 2014; G. Gozaliasl et al. 2025; L. Yang et al. 2025). Because stellar mass reflects the combined effects of internal physics and environmental processes, it is an essential parameter for tracing the imprint of these influences and for bridging galaxy-scale processes with the large-scale cosmic web. Moreover, SFR measures the current rate of stellar-mass growth (R. C. Kennicutt 1998; P. Madau & M. Dickinson 2014; L. J. Tacconi et al. 2020) and reflects feedback processes that regulate the gas reservoir and suppress subsequent star formation (P. F. Hopkins et al. 2012; T. Naab & J. P. Ostriker 2017; R. Maiolino & F. Mannucci 2019; Z. Ghaffari et al. 2026). Thus, investigating how SFR evolves across different environments helps clarify the role that external conditions play in galaxy evolution.

Part of the observed dependence of SFR on environment is driven by quenching, rather than changes in the SFR itself (N. Chartab et al. 2020; S. Taamoli et al. 2024a). Both stellar mass and environment can control quenching (Y.-j. Peng et al. 2010). Internal mechanisms such as AGN feedback, morphological stabilization, and shock heating tend to suppress star formation in massive galaxies (A. Dekel & Y. Birnboim 2006; M. Martig et al. 2009; K. Schawinski et al. 2014). External mechanisms including ram pressure stripping, strangulation, and galaxy interactions act in dense environments to remove or heat gas and halt star formation (J. E. Gunn & J. R. Gott 1972; B. Moore et al. 1999; A. R. Wetzel et al. 2013; B. M. Poggianti et al. 2017). Recent studies show that mass and environmental quenching efficiencies both increase with stellar mass, with mass quenching dominating at the high-mass end and environmental effects becoming more important for low-mass systems, particularly at low redshift (N. Chartab et al. 2020; S. Jin et al. 2024; S. Taamoli et al. 2024b). Therefore, stellar-mass growth, ongoing star formation, and the quenching processes that shut down star formation are all connected to each other. Stellar mass traces the cumulative history of star formation, while the SFR reflects the current level of activity, and the specific SFR (sSFR $\equiv$ SFR$/M_*$) links the two by showing the relative pace of growth. Physical mechanisms behind quenching regulates how and when this growth is halted, and its strength depends on both internal factors related

to mass and external influences from the environment. Understanding how these trends depend on environment is therefore a multidimensional problem, requiring all of these parameters to be considered simultaneously.

At high redshift, observational limitations led to mixed results in previous studies. Some studies find a weakening or flattening of the SFR relation with density (N. Scoville et al. 2013; B. Darvish et al. 2016), others report no significant correlation (R. Grützbauch et al. 2011), and some detect enhanced star formation in dense environments at $z \gtrsim 2$ (D. Elbaz et al. 2007; B. C. Lemaux et al. 2022). The release of COSMOS2020, with its deeper photometry and improved photometric redshifts, extended such measurements to $z \lesssim 4$ (J. R. Weaver et al. 2022; S. Taamoli et al. 2024a). However, even with these advances, samples remain highly biased at the highest redshifts, particularly for low-mass galaxies, where photometric uncertainties and selection effects influence both the completeness and reliability of environmental trends (M. Brinch et al. 2023; S. Taamoli et al. 2024a).

To overcome these depth and completeness limitations, COSMOS-Web was designed to provide the first wide-area JWST-based view of the cosmic web, covering 0.54 deg^2 of the COSMOS field with NIRCam imaging and complementary MIRI observations (C. M. Casey et al. 2023). Its area is sufficiently wide to capture the full diversity of the cosmic web, and its near-infrared depth (reaching 5σ depths of 27.2–28.1 AB mag) pushes detections to $z \sim 10$ (C. M. Casey et al. 2023, 2024; M. Shuntov et al. 2025a; M. Franco et al. 2026). COSMOS-Web provides a mass-selected sample, reaching 80% completeness at $\sim 10^9\,M_\odot$ at $z \sim 10$ (M. Shuntov et al. 2025a). These advances improve the accuracy of LSS reconstructions and extend environmental studies to higher redshifts than previously possible (G. Toni et al. 2025; D. Scognamiglio et al. 2026).

This paper focuses on the LSSs identified from the COSMOS-Web survey—the first wide-area, deep, near-infrared-selected survey designed to study the cosmic web and the impact of environment on galaxy properties. This paper is structured as follows. In Section 2, we describe our dataset and sample selection. In Section 3, we describe the method we used to measure density maps. In Section 4, we present the density map results. In Section 5, we compare our results from COSMOS-Web with COSMOS2020, then discuss our results for the evolution of galaxy properties with the cosmic web. Finally, we summarize our findings in Section 6.

In this work, we adopt a flat ΛCDM cosmology with $H_0 = 70\,\mathrm{km\,s^{-1}\,Mpc^{-1}}$, $\Omega_{\mathrm{m},0} = 0.3$, and $\Omega_{\Lambda,0} = 0.7$. All magnitudes are expressed in the AB system (J. B. Oke 1974), and a Chabrier initial mass function is assumed (G. Chabrier 2003).

2. Data

2.1. COSMOS-Web

The COSMOS-Web survey (C. M. Casey et al. 2023) provides deep JWST observations in the central 0.54 deg^2 of COSMOS in four NIRCam bands (F115W, F150W, F277W, and F444W), reaching a 5σ point-source depth of 27.5–28.2 mag. In addition, MIRI F770W covers ∼0.20 deg^2, with a 5σ depth of 25.3–26.0 mag (G. S. Wright et al. 2023). The data reduction for NIRCam and MIRI are described in M. Franco et al. (2026) and S. Harish et al. (2025), and the photometric catalog is presented in M. Shuntov et al. (2025a). The COSMOS-Web catalog contains about 780,000 galaxies, with roughly 80% completeness at $\log(M_\star/M_\odot) \sim 9$ by $z \sim 10$ and $\log(M_\star/M_\odot) \sim 7$ by $z \sim 0.2$—an improvement of about 1 dex compared to COSMOS2020. The combination of depth, area, and full multiwavelength coverage makes COSMOS-Web the most powerful dataset to study galaxy formation and evolution up to high redshifts ($z \sim 7$).

2.2. COSMOS2020

To directly assess the improvements of COSMOS-Web in LSS studies relative to previous surveys, we use the COSMOS2020 catalog, which provides multiwavelength photometry over the full 2 deg^2 of the COSMOS field (J. R. Weaver et al. 2022). It combines imaging from over 30 bands spanning 0.3–8 μm, coming from a range of ground- and space-based observatories. The optical imaging includes broadband (g, r, i, z, y) data from Subaru/Hyper Suprime-Cam (HSC), 11 mediumband and 2 narrowband filters from Subaru/Suprime-Cam that were originally obtained for COSMOS2015 and subsequently incorporated into COSMOS2020 (Y. Taniguchi et al. 2007, 2015; C. Laigle et al. 2016; H. Aihara et al. 2022; J. R. Weaver et al. 2022), and CFHT/MegaCam u-band imaging from the CLAUDS program (M. Sawicki et al. 2019). Near-infrared data are provided by UltraVISTA DR6 from VISTA/VIRCAM (H. J. McCracken et al. 2012; W. Sutherland et al. 2015). Space-based data include Hubble Space Telescope/Advanced Camera for Surveys F814W (A. M. Koekemoer et al. 2007, 2011) and Spitzer/IRAC mid-infrared imaging (D. B. Sanders et al. 2007; M. L. N. Ashby et al. 2018).

The COSMOS2020 release provides two complementary catalogs, the "CLASSIC" catalog, based on aperture photometry, and the `Farmer` catalog, produced with the `Farmer` profile-fitting tool (J. R. Weaver et al. 2022). The `Farmer` catalog measures total fluxes without aperture corrections and models blended sources more effectively, especially in low-resolution images, such as those from IRAC. In contrast, `CLASSIC` aperture photometry tends to underestimate the total flux and cannot model blended objects simultaneously. Although the photo-z quality is similar between the two, `Farmer` performs better at fainter magnitudes ($i \geqslant 24$), which mainly correspond to high-redshift galaxies. For our density estimates, we use photometric redshifts and galaxy properties derived from the `Farmer` measurements using `LePhare` spectral energy distribution (SED) fitting (J. R. Weaver et al. 2022).

2.3. Sample Selection

We define selection criteria for the COSMOS-Web and COSMOS2020 catalogs to construct density maps, ensuring the samples are as complete as possible and directly comparable for evaluating JWST's improvements in LSS mapping. At low redshift, the catalogs include large numbers of low-mass galaxies that are not detectable at higher redshift. Having such galaxies in the density reconstruction only at low z would change the tracer population with redshift and bias comparisons of the LSS evolution. For this reason, we adopt a constant stellar-mass threshold rather than a redshift-dependent one. We estimate the stellar-mass completeness limit for the COSMOS-Web catalog following the method of L. Pozzetti et al. (2010) and M. Shuntov et al. (2025b), by rescaling stellar masses to the total F444W magnitude limit of

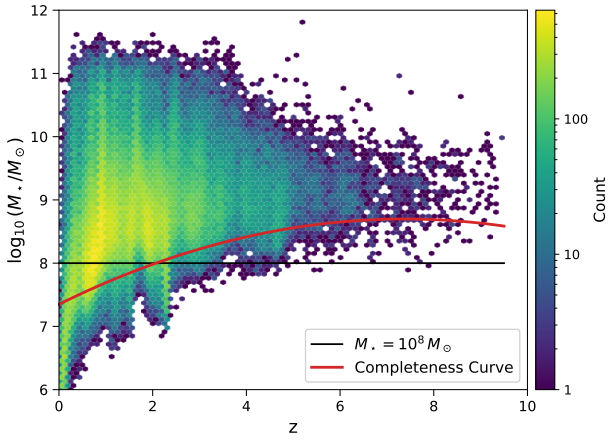

Figure 1. Galaxy stellar mass as a function of redshift. The red curve shows the stellar-mass completeness limit derived following the method of L. Pozzetti et al. (2010), obtained by rescaling stellar masses to the total F444W magnitude limit of the survey (27.5) and taking the 90th percentile of the resulting distribution in each redshift bin. The solid red line represents the best-fit polynomial in $(1 + z)$. The black line marks the stellar-mass threshold of $\log(M_\star/M_\odot) = 8$ used in our sample selection.

the survey (27.5; M. Shuntov et al. 2025a) and taking the 90th percentile of the resulting distribution in each redshift bin. The red curve in Figure 1 shows this completeness function, and the black line illustrates the mass cut. The sample remains complete down to $\log(M_\star/M_\odot) \sim 8.5$ at $z \sim 7$. Based on the COSMOS-Web catalog, we select galaxies with $\log(M_\star/M_\odot) = 8$. This threshold lies close to the completeness boundary over most of the redshift range. Lowering the threshold would introduce a strongly redshift-dependent tracer population, while raising it would remove a substantial fraction of low-redshift galaxies and dilute the density field. We quantify the impact of this choice by comparing the constant cut to a redshift-dependent completeness limit. A threshold of $\log(M_\star/M_\odot) = 8$ excludes only $\sim$10% of the galaxies that would be retained by a variable cut at low redshift, whereas increasing the threshold to $\log(M_\star/M_\odot) = 8.5$ would remove $\sim$30% of the sample. For a constant threshold of $\log(M_\star/M_\odot) = 8$, the difference between the stellar-mass limits at low and high redshift is $\lesssim$0.5 dex (Figure 1 and Table 2), whereas adopting a redshift-dependent threshold leads to a separation of more than 1 dex between the low- and high-redshift mass limits (Figure 1), making this the lowest constant threshold that preserves statistics while limiting redshift-dependent selection effects.

With a magnitude limit of $K_s = 24.5$ (AB) on the COSMOS2020 catalog, the sample is complete to $i \approx 24.9$ (AB), and $\sim$32% of the sources lie in the range $24 \leqslant i \leqslant 24.9$ where `Farmer` performs better. The main limitation of `Farmer` is that it cannot model sources near bright objects, leading to the exclusion of $\sim$16% of sources in the star-masked areas. We discard all objects near stars, `STAR_HSC` masked regions, to make sure the photometric redshifts are accurate and reliable (J. Coupon et al. 2018). We also exclude objects with bad SED fittings (χ^2/number of filters used < 3; C. M. Casey et al. 2024). We set a magnitude limit of 27.35 for F150W for the COSMOS-Web catalog (G. Toni et al. 2025). In order to have reliable redshift estimates, we only use galaxies with $\sigma_z/(1 + z) < 0.1$ for both catalogs (S. Taamoli et al. 2024a). After applying all these criteria, COSMOS-Web remains with $\sim$164,000 galaxies, and COSMOS2020 narrows down to $\sim$79,000 galaxies. The sample selection criteria are summarized in Table 1.

3. Density Estimation Method

In photometric surveys, an appropriate density estimator must account for redshift uncertainties, incomplete sampling, and survey geometry, while producing a projected density field from discrete galaxy tracers. The environmental density can be estimated using various methods, including weighted kernel density estimation (wKDE), weighted k-nearest neighbors, weighted Voronoi tessellation, and weighted Delaunay triangulation. Based on the comparison of these methods by B. Darvish et al. (2015), wKDE and Voronoi tessellation best reproduce the density field in simulations, with wKDE showing higher stability against shot noise and sparse sampling. We reconstruct the environmental density field using the wKDE method developed by B. Darvish et al. (2015), as adapted and applied in recent studies (N. Chartab et al. 2020; M. Brinch et al. 2023, 2024; S. Taamoli et al. 2024a). This approach uses wKDE over photometric redshift slices, considering galaxy redshift uncertainties and correcting for survey geometry and masking. We use the same method for both catalogs and describe it below.

3.1. Redshift Slicing Based on Physical Scale

We define redshift slices based on a fixed comoving thickness of $\Delta\chi = 35\,h^{-1}$ Mpc. This physical scale is chosen to be larger than the characteristic sizes of galaxy groups and clusters and sufficiently wide to encompass redshift-space distortions and photometric redshift errors (S. I. Muldrew et al. 2015).

The redshift width Δz for each slice is computed using

$$\Delta z = \frac{H_0}{c}(1 + z)\sqrt{\Omega_{m,0}(1 + z)^3 + \Omega_{\Lambda,0}} \times \Delta\chi. \quad (1)$$

As a consequence of the redshift dependence of Δz and the adopted definition of the slice centers, adjacent redshift slices slightly overlap, typically at the level of $\Delta z \sim 10^{-4}$. This results in 157 slices spanning $z = 0.4$ to $z = 9.5$, with Δz varying from $\sim$0.014 at $z = 0.4$ to $\sim$0.208 at $z = 9.5$. However, density maps of COSMOS-Web can only be reliable up to $z \sim 7$, which we will discuss in detail in Section 4.4. The remaining slices are only considered as buffers for redshift probability distribution functions (PDFs), to have more reliable weights, and for more accurate density estimation at higher redshifts.

3.2. Redshift Probability Weighting

Each galaxy contributes to multiple redshift slices according to its photometric redshift PDF, $P(z)$. The weight of a galaxy g in slice s is given by

$$w_g^s = \int_{z_s^{\min}}^{z_s^{\max}} P_g(z)\, dz, \quad (2)$$

where the integration is over the bounds of slice s. For galaxies with unimodal PDFs, $P(z)$ is approximated as a Gaussian centered at the photo-z, with σ_z equal to the 68% confidence interval (C. Laigle et al. 2016). To reduce computation time, we apply a weight threshold $w_{\rm th} = 0.05$, recommended by S. Taamoli et al. (2024a), meaning galaxies contribute to a slice only if $w_g^s > 0.05$.

Table 1
Selection Thresholds and Filtering Criteria Applied to COSMOS-Web and COSMOS2020 Catalogs for Density Field Construction

Selection Criterion	COSMOS-Web	COSMOS2020
Sky Area	COSMOS-Web 0.54 deg^2 area	Limited to COSMOS-Web area (to avoid edge effects)
Magnitude Limit	F150W < 27.35	$K_s < 24.5$
Redshift Limit	$z < 9.5$	$z < 6.0$
Stellar-mass Cut ($M_\odot$)	10^8	10^8
Photometric Redshift Quality	$\sigma_z/(1+z) < 0.1$	$\sigma_z/(1+z) < 0.1$
SED Fitting Quality	$\chi^2/N_{\rm filters} < 3$	$\chi^2/N_{\rm filters} < 3$
Star Mask	`STAR_HSC` excluded	`STAR_HSC` excluded

3.3. KDE with von Mises–Fisher Kernel

We estimate the surface density field $\sigma^s(\boldsymbol{X})$ in each redshift slice s using a wKDE:

$$\sigma^s(\boldsymbol{X}_i) = \sum_g w_g^s \, K(\boldsymbol{X}_i; \boldsymbol{X}_g, b_g), \tag{3}$$

where $\boldsymbol{X}_i$ and $\boldsymbol{X}_g$ denote the angular coordinates of the target and contributing galaxies, w_g^s is the redshift weight, and b_g is the adaptive kernel bandwidth. The kernel function is chosen to be the von Mises–Fisher (vMF) distribution (N. Chartab et al. 2020), a spherical analog to the Gaussian:

$$K(\boldsymbol{X}_i; \boldsymbol{X}_g, b) = \frac{\exp(\cos(\psi)/b^2)}{4\pi b^2 \sinh(1/b^2)}, \tag{4}$$

where ψ is the angular separation between $\boldsymbol{X}_i$, and $\boldsymbol{X}_g$. b is the bandwidth of the vMF kernel, which shows how much a galaxy at $\boldsymbol{X}_g$ can affect the density at $\boldsymbol{X}_i$. This kernel naturally handles angular coordinates and becomes equivalent to a Gaussian for small ψ.

3.4. Bandwidth Selection

To balance the smoothing and spatial resolution, we determine the optimal global bandwidth b_s for each redshift slice using the leave-one-out likelihood cross-validation (LCV) method (P. Hall 1982; N. Chartab et al. 2020). This method tests different bandwidths and selects the one that best predicts the density at each galaxy's position when that galaxy is left out. In practice, this means identifying the smoothing scale for which the local surface density inferred from neighboring galaxies most consistently reproduces the observed galaxy distribution, without being dominated by shot noise or oversmoothing. LCV is given by

$$\mathrm{LCV}(b) = \sum_{k=1}^{N} \log \sigma^s_{-k}(\boldsymbol{X}_k), \tag{5}$$

where σ^s_{-k} excludes the galaxy k when computing the density at $\boldsymbol{X}_k$. The value of b_s that maximizes this expression is chosen as the global bandwidth for that slice.

After determining the bandwidth of each slice, b_s, we assign each galaxy its own adaptive bandwidth b_g, based on the local density. In dense regions, we reduce the bandwidth to capture finer structures; in sparse regions, we increase it to reduce noise:

$$b_g = b_s \left(\frac{\bar{\sigma}}{\sigma^s(\boldsymbol{X}_i)} \right)^{\alpha}, \tag{6}$$

with $\bar{\sigma}$ being the mean surface density in the slice and $\alpha = 0.5$, as recommended in I. S. Abramson (1982). This allows the smoothing scale to adjust, based on the environment, to improve the overall quality of the density field by enhancing the reconstruction of coherent LSSs while suppressing spurious fluctuations driven by sparse sampling and photometric redshift uncertainties, with small-scale density contrasts preserved in highly structured regions.

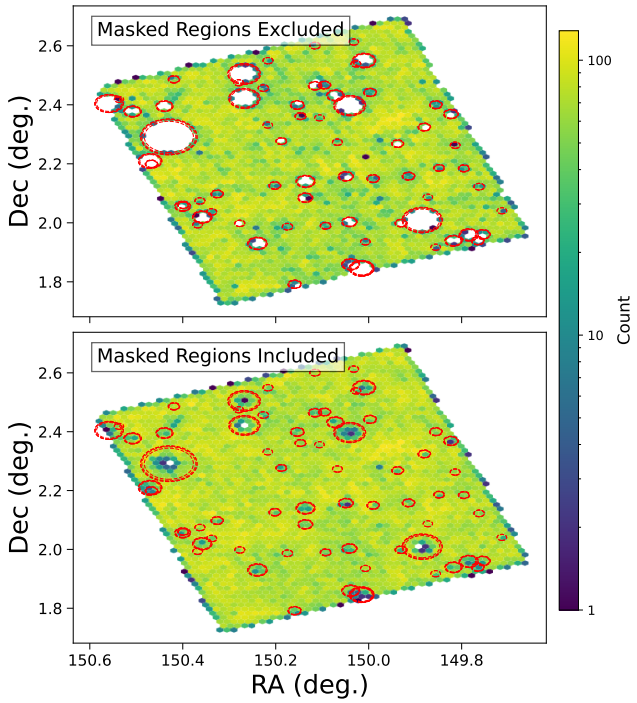

Figure 2. Count of COSMOS-Web sources after all selection cuts. The red dashed circles show HSC masked regions. Top: masked regions excluded. Bottom: masked regions included. Keeping detections inside the masks still leaves low number density inside the red circles, which would bias our LSS analysis.

3.5. Correction for Masked Regions

In widefield surveys such as COSMOS, bright stars and image artifacts contaminate large areas of the field, producing regions where photometry and SED fits are unreliable. These regions are masked, and the galaxies within them are excluded from the catalogs. If left uncorrected, such masks introduce systematic underdensities in the reconstructed density field, and large masks can mimic void-like structures that are not physically real. This effect becomes especially problematic when tracing LSS, since density fluctuations on scales comparable to the mask size may be dominated by these observational artifacts rather than true cosmic variance.

Figure 2 shows the distribution of all sources in the COSMOS-Web field—one panel including all detected

galaxies and one excluding those in the HSC mask. Even when galaxies within masked regions are included, their median detection rate is about 30% lower, producing underdensities that resemble physical voids. This demonstrates the need to exclude sources in these regions and apply a correction to account for the masked regions.

To mitigate the effect of these regions, we follow the approach of S. Taamoli et al. (2024a) and fill the masked regions with a uniform distribution of artificial sources. For each redshift slice s, we assign a mean number density equal to the surface density of galaxies in the unmasked area of the field:

$$\bar{n}_s = \frac{\sum_g w_g^s}{A_{\rm field} - A_{\rm masked}}, \tag{7}$$

where $A_{\rm field}$ is the total field area and $A_{\rm masked} = 0.127\,A_{\rm field}$ is the masked area. This correction ensures that masked regions contribute neutrally to the density field, preventing spurious underdensities and yielding smoother and more physically consistent maps of LSS.

3.6. Edge Correction

Galaxy densities near the boundaries of the observed field are underestimated, because part of the smoothing kernel extends outside the region covered by the catalog and therefore contributes no galaxies. To account for this, we calculate the effective fraction of the kernel that remains inside the observed field. For a galaxy at position $\boldsymbol{X}_i$, this fraction is

$$\eta(\boldsymbol{X}_i) = \int_{\rm field} K(\boldsymbol{X}_i; \boldsymbol{X})\, d\boldsymbol{X}, \tag{8}$$

where the integration is restricted to the observed field area. Physically, $\eta(\boldsymbol{X}_i)$ measures how much of the kernel centered at $\boldsymbol{X}_i$ lies within the data region. Well inside the field, the kernel is fully contained, and $\eta(\boldsymbol{X}_i) \approx 1$. Near the edges, a portion of the kernel lies outside the field, giving $\eta(\boldsymbol{X}_i) < 1$. Dividing the raw density by $\eta(\boldsymbol{X}_i)$ renormalizes the estimate, so that edge galaxies are treated consistently with those in the interior:

$$\sigma^s_{\rm corrected}(\boldsymbol{X}_i) = \frac{\sigma^s(\boldsymbol{X}_i)}{\eta(\boldsymbol{X}_i)}. \tag{9}$$

This procedure corrects the systematic underestimation at field boundaries and yields reliable density estimates across the entire map (M. C. Jones 1993; N. Chartab et al. 2020).

3.7. Density Contrast Field

We define the dimensionless density contrast as

$$\delta = \frac{\sigma^s_{\rm corrected}(\boldsymbol{X}_i) - \bar{\sigma}^s}{\bar{\sigma}^s}, \tag{10}$$

where $\bar{\sigma}^s$ is the mean surface density in the slice. The final result is a set of 157 angular density fields and corresponding density contrast maps spanning $z = 0.4$ to 9.5.

4. Results

In this section, we present the results for each step of our method. We first show how galaxies are distributed across redshift slices defined by a fixed width of $35\,h^{-1}$ Mpc. We then present the results for the bandwidth selection, edge correction, and density fields in the COSMOS-Web field. Last, we assess the highest redshift at which our density measurements remain reliable for the purpose of our work.

4.1. Redshift Distribution

The distribution of galaxies in different redshift slices and their normalized photometric redshift uncertainties are shown in Figure 3. The top panel displays the histogram of galaxies as a function of redshift. Each redshift bin corresponds to a slice used for constructing the density maps Galaxies that contribute to each slice with a weight of $w_g^s > 0.05$ based on their redshift PDF are considered for building the density maps. At higher redshifts (e.g $z > 6$), the number of galaxies is lower than later epochs, due to observational limits.

Normalized redshift uncertainties remain relatively low at $z < 6.5$ and gradually increase toward higher redshifts. While the median $\sigma_z/(1+z)$ remains below typical quality thresholds across all redshifts, uncertainties grow at high redshift, because of a lower photometric signal-to-noise ratio and the smaller number of filters in which galaxies are detected, which limits the constraints on their SEDs. This naturally impacts the precision of the density estimates at those epochs.

Nevertheless, our approach incorporates the photometric redshift uncertainty for each galaxy, ensuring that the density field reconstruction reflects the underlying redshift uncertainties. This enables the detection of LSS even at high redshift, though with decreasing spatial resolution and greater uncertainty.

4.2. Density Field Maps

We visualize the step-by-step construction of the density field in Figure 4 for one representative redshift slice at $z \sim 3.7$. Each panel demonstrates a component of the wKDE method explained in Section 3. These intermediate maps allow us to evaluate the quality of the inputs and better understand the reliability of the final density construction.

In the top left panel, we show the spatial distribution of galaxies within the slice, color-coded by their redshift weight contributions w_g^s. The masked regions (`STAR_HSC`) have been filled by the average density of the field, to avoid introducing artificial underdensities near bright stars. These added objects have a mean weight value of all the galaxies in the slice.

The top right panel shows the spatial variation of the adaptive kernel bandwidth b_i. Smaller bandwidths are assigned to dense regions, where the tracer sampling supports finer spatial resolution, while larger bandwidths are used in underdense regions, to suppress fluctuations caused by sparse sampling. This adaptivity allows the reconstruction to preserve compact overdensities while maintaining stable estimates in more diffuse regions; it is particularly important at higher redshift, where sparser sampling requires additional smoothing, to suppress shot noise and yield a more reliable reconstruction of the large-scale density field.

The bottom left panel displays the boundary correction factor η, which accounts for edge effects and ensures that density values near the boundary regions are not underestimated due to truncated kernels. In the center of the field, where the full kernel fits inside the survey area, η is close to 1. Near the edges, where only part of the kernel overlaps with the data, η increases to around 2. In the corners, where most of the kernel is outside the field, η can approach 4.

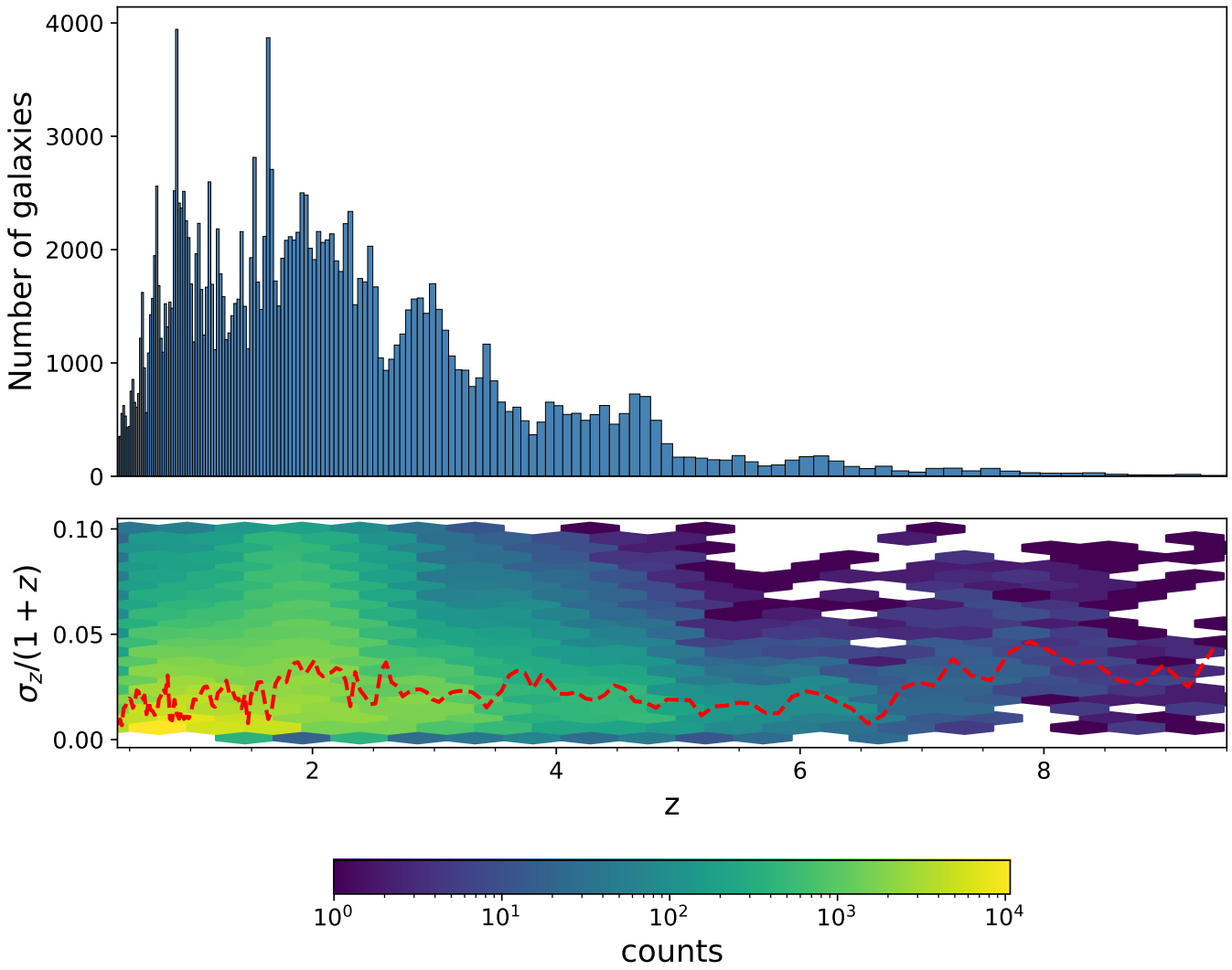

Figure 3. Top: redshift distribution of galaxies in the COSMOS-Web sample. Each bin corresponds to a redshift slice used in the density field reconstruction. Bottom: normalized photometric redshift uncertainty, $\sigma_z/(1+z)$, as a function of redshift. The color map shows the number of galaxies at each redshift uncertainty bin on a logarithmic scale. The red dashed line shows the median uncertainty in each redshift slice.

Finally, the bottom right panel presents the output density field. It is visualized with the dimensionless overdensity $1+\delta$. These maps are generated for all redshift slices, and we use them to assign a density contrast value to each galaxy in the field. Figure 5 shows the evolution of these 2D density maps with redshift in the COSMOS-Web field. Together, these figures show that the wKDE method recovers coherent structure even at early times, allowing us to connect galaxy properties to their environments over most of cosmic history. At the highest redshifts, extended regions of elevated $1+\delta$—such as the feature spanning $\sim 0.5^\circ$ in the $z \sim 6.7$ slice—trace large-scale density gradients in projection rather than physically bound systems. Such features are expected, given the sparse sampling and early stage of structure growth at these epochs, and do not imply the presence of a single massive cluster progenitor. For a qualitative cross check with known structures, we overlay protocluster and group candidates from the COSMOS-Web deep galaxy group catalog of G. Toni et al. (2025), which extends to redshift $z \sim 3.7$. Candidates are selected using the Adaptive Matched Identifier of Clustered Objects detection metric S/N^{nocl}, and we adopt a threshold of $S/N^{nocl} > 7$, which corresponds to a purity of approximately 80% for that catalog (G. Toni et al. 2025). For each redshift slice, we include only those candidates whose reported redshift uncertainty interval overlaps the slice. The pixels associated with these group and protocluster candidates have mean $1+\delta$ values that are typically about 50% higher than the slice average, indicating that the highest overdensities in our field spatially coincide with known group and protocluster candidates. Intermediate values of δ are therefore expected to correspond statistically to filament-like regions, while the lowest δ values likely trace galaxies in void-like environments. A quantitative calibration between δ and a full classification of nodes, filaments, and voids based on the Hessian of the density field requires a dedicated analysis and could be explored in future work.

4.3. Density Contrast of Galaxies

After generating overdensity maps for each slice in COSMOS-Web, we find the overdensity associated with each galaxy in the field. Figure 6 shows the distribution of $\log(1+\delta)$ as a function of redshift. At lower redshifts ($z \lesssim 2$), galaxies span a wider range of overdensities. They vary from very low underdensities to strong overdensities.

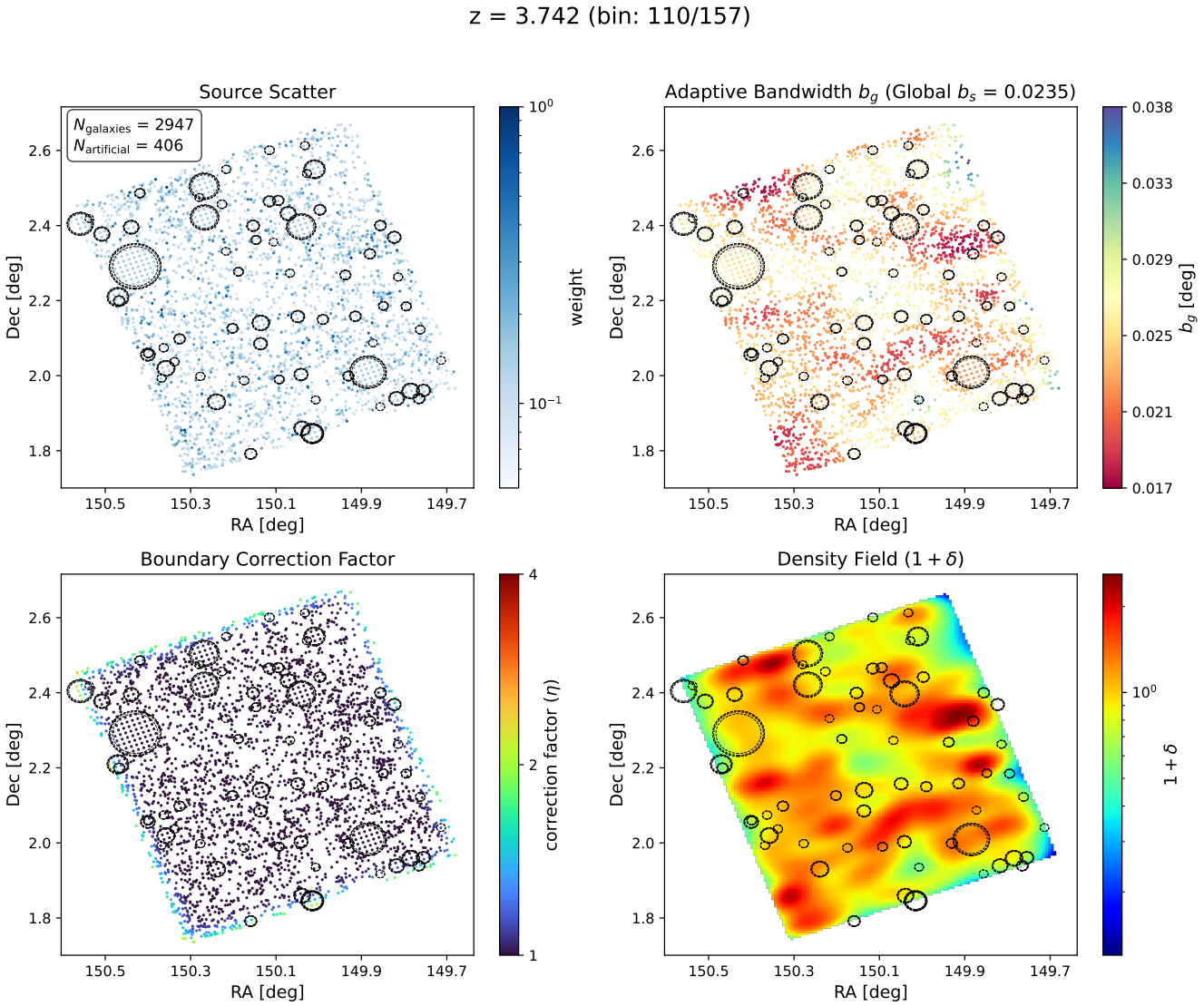

Figure 4. Steps in the construction of the density field for a redshift slice at $z \sim 3.7$. Top left: distribution of galaxies and artificial sources colored by their weight. Top right: adaptive bandwidth assigned to each galaxy. Bottom left: boundary correction factor η applied near survey edges. Bottom right: final density field $1 + \delta$. The circles show the HSC masked regions.

(The complete figure set (143 images) is available in the online article.)

This is expected, as LSS is more evolved at later times, with well-formed clusters and filaments becoming more prominent.

As the redshift increases, the number of galaxies decreases, and the overall spread in $\log(1 + \delta)$ narrows. This is consistent with both the lower number density of galaxies in the early Universe and the increased difficulty of resolving the structures. However, a significant range of density contrast remains detectable even at higher redshifts, with galaxies present in both relatively overdense and underdense regions. The decrease in counts at high redshifts is due to the intrinsic rarity of detectable galaxies at early epochs. However, our selection criteria ensure reliable redshifts and SED fits in this range.

At lower redshifts, overdense regions typically correspond to matured environments, such as clusters and filaments. These are epochs during which galaxies experience strong environmental effects. In contrast, at higher redshifts, the same values of $\log(1 + \delta)$ do not imply the same level of structural maturity. It is important to note that the interpretation of overdensities and underdensities changes with cosmic time. At lower redshifts, LSS overdensities typically correspond to well-defined gravitationally bound structures, such as clusters, filaments, and walls. At higher redshifts ($z > 1.5$), overdense regions are usually associated with structures that are still in the process of formation, such as protoclusters or early filaments and walls that have not yet reached their full structural development (Y.-K. Chiang et al. 2013; S. I. Muldrew et al. 2015). This context is important for interpreting how galaxy properties relate to environment across redshift. For this reason, we do not interpret a given overdensity percentile at high redshift as the direct physical counterpart of the same percentile at low redshift. Instead, our analysis is explicitly within-epoch. In each redshift bin, we measure the dependence of stellar mass, SFR, sSFR, and quenching with overdensity, see how the strengths and signs of these within-bin correlations change, then compare the trends between different redshifts. In our 2D analysis of the cosmic web, filaments that are elongated in the line of sight can appear like clusters, and edge-on cosmic walls may appear as filaments due to projection. Additionally, photometric redshift estimates can introduce artificial accumulations at certain

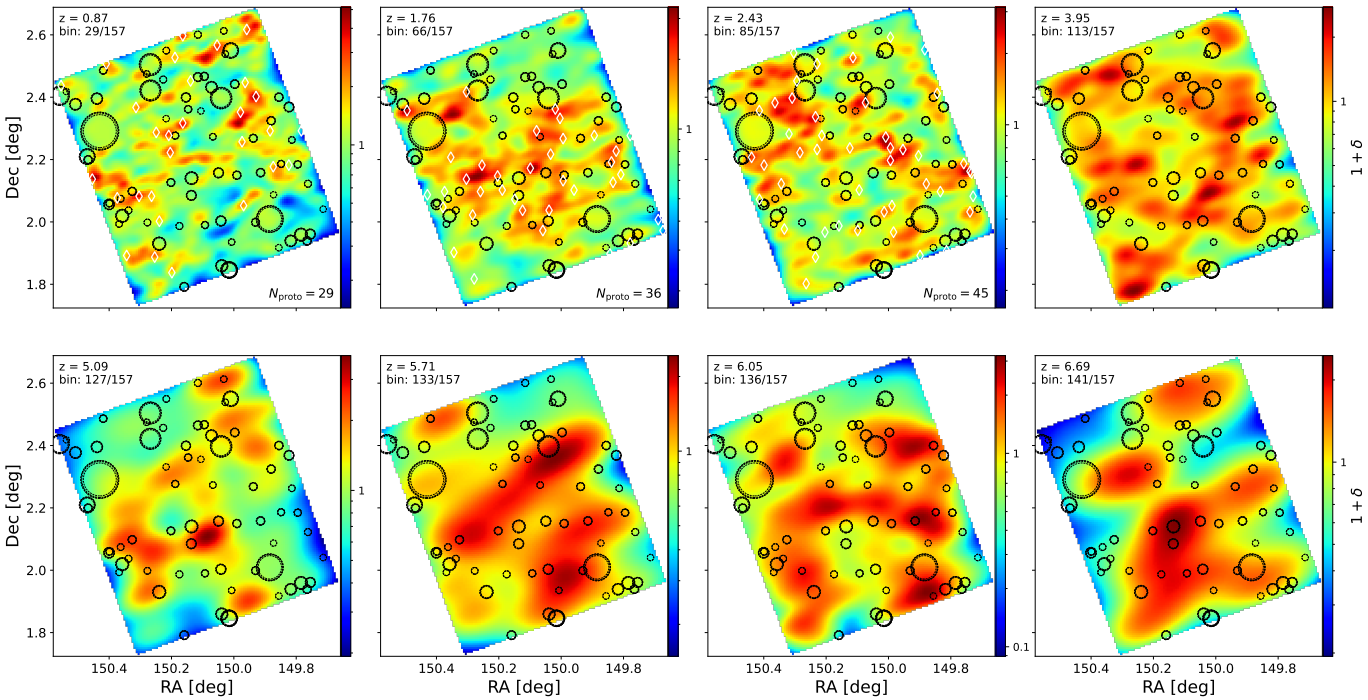

Figure 5. Evolution of overdensity maps in the COSMOS-Web field across cosmic time. Each panel shows the overdensity field for a fixed comoving slice; the color bars are scaled independently in each redshift bin. While absolute overdensity amplitudes cannot be directly compared across panels, the maps illustrate the changing topology and distribution of LSS with increasing redshift. The circles mark the HSC star-masked regions. The white diamond markers indicate protocluster and group candidates from the COSMOS-Web deep galaxy group catalog of G. Toni et al. (2025), which goes up to redshift $z \sim 3.7$, selected with $S/N^{nocl} > 7$, corresponding to an approximately 80% purity level. Markers are included only when the candidate redshift uncertainty interval overlaps the slice.

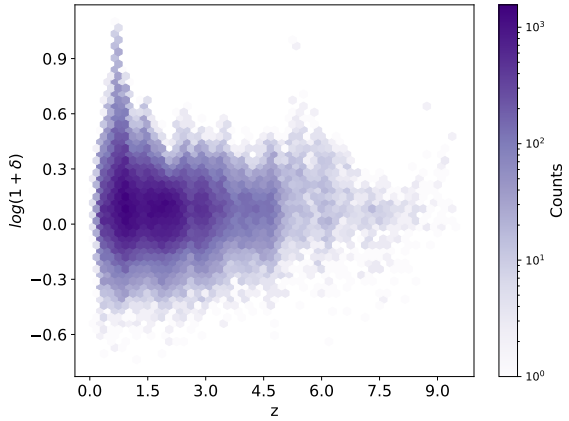

Figure 6. Distribution of galaxy overdensity, $\log(1+\delta)$, as a function of redshift in COSMOS-Web. The colors show the number of sources in each bin. The scatter of $\log(1+\delta)$ is broad at $z \lesssim 2$, spanning low underdensities to high overdensities. The distribution narrows as redshift increases. Near $z \sim 5$, the low-density tail compresses and galaxies occur more often in overdense regions, and by $z \sim 7$ the high-density end is suppressed.

redshifts, leading to spurious enhancements or depletion in the apparent galaxy number density. Such effects are modest, but should be kept in mind when interpreting the redshift–overdensity distribution.

To provide a complementary view, Figure 7 shows a thin slice of COSMOS-Web in comoving coordinates. This diagram shows how galaxies trace LSSs over cosmic time, from the nearby Universe out to the highest redshifts probed. Galaxies in overdense regions are in filaments, groups, clusters, or protoclusters, while those in underdense regions populate voids, providing the framework in which their physical properties (such as stellar mass, SFR, or sSFR) can be studied as a function of environment. These overdensity maps in the COSMOS-Web field thus serve as a powerful tool for investigating how galaxies evolve across environments and how early LSS may influence stellar-mass growth and star formation activity, which will be discussed in detail in Section 5.

4.4. Maximum Reliable Redshift

The maximum reliable redshift depends on the scientific context. Whether the density fields are sufficient for studying correlations between galaxy properties and large-scale environments depends on the intended study. This is inherently a more qualitative threshold, but the coherence of density maps with adaptive bandwidth and statistical trends in overdensity values is important. Also, sample selection can affect the density fields, especially at higher redshifts.

We evaluate the reliability of the density reconstruction at high redshift using a combination of quantitative diagnostics and structural consistency checks. First, we examine the evolution of the overdensity distribution (Figure 6). In Figure 6, as the redshift increases, the distribution of $\log(1+\delta)$ gradually narrows. Around $z \sim 5$, the low-density tail compresses, and galaxies are found more frequently in overdense regions. Then, by $z \sim 7$, we observe that the high-density end becomes suppressed, and the detected galaxies in our sample mostly occupy intermediate-density regions. This shift may be partially affected by a bias in the sample at higher redshifts, due to reionization, but it may reflect an early growth stage of LSS. These trends show that while environmental structure exists at high redshift, the contrast between overdense and underdense regions diminishes, which limits how precisely we can define a galaxy's environment.

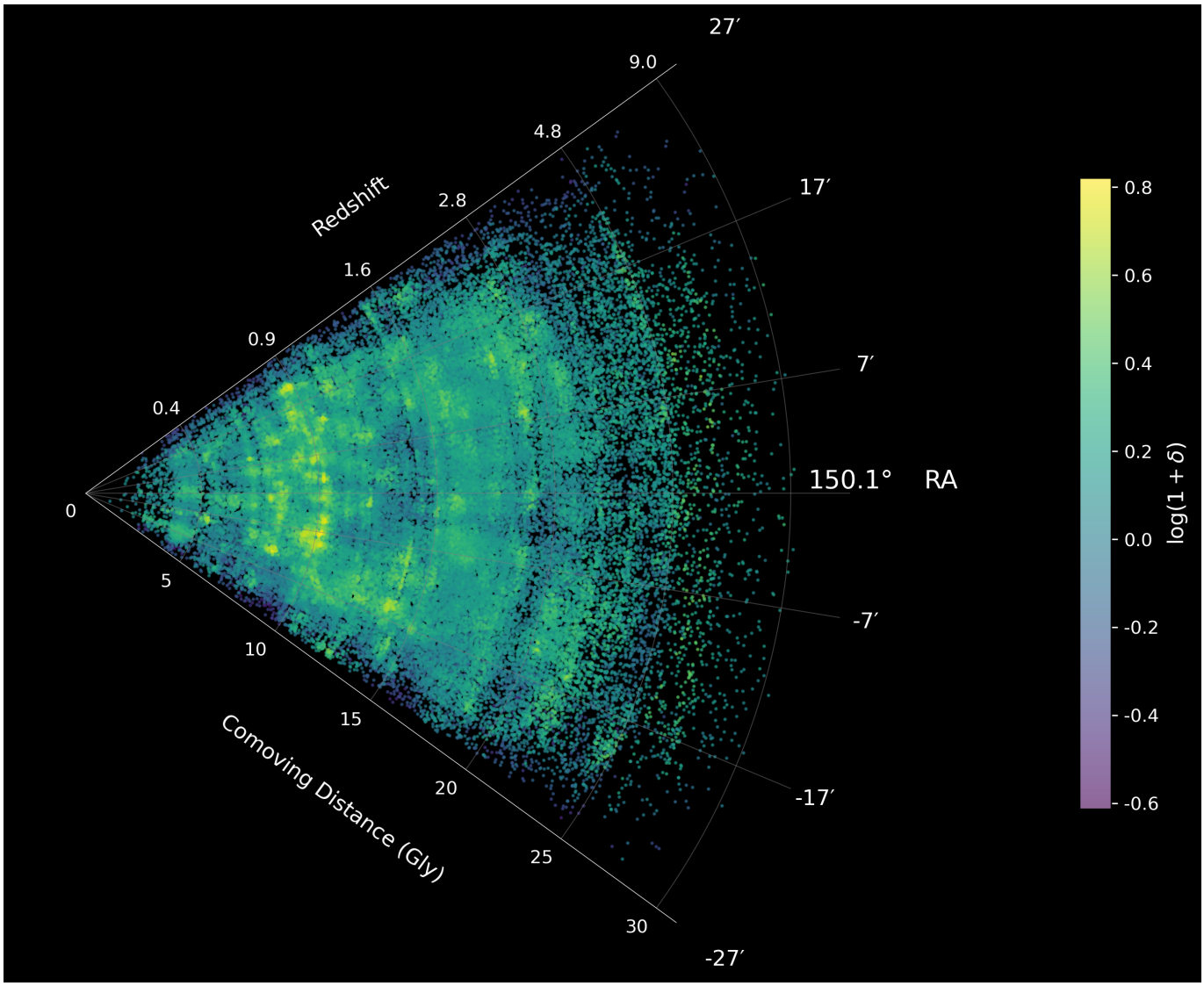

Figure 7. A slice of COSMOS-Web showing the LSS of galaxies. The plot selects galaxies within a $\Delta\mathrm{decl} \sim 0.^{\circ}5$ band centered on the field median. The lower and upper radial coordinates give the comoving distance in Gly and redshift, and the angular extent corresponds to R.A. offsets of $\pm 27'$ from the field center at R. A. $= 150.^{\circ}1$. Each point is color-coded by local overdensity, expressed as $\log(1 + \delta)$.

Second, we consider the decline in the effective tracer number density with redshift. Although the redshift precision remains controlled through our selection criteria ($\sigma_z/(1+z) < 0.1$) and high-quality SED fits, the average value of $\sigma_z/(1+z)$ and the total number of galaxies per slice decrease toward higher redshift. This reduced sampling limits the construction of the density field.

Third, we evaluate the spatial coherence of the reconstructed density maps. We visually inspect the density fields at high redshifts, to determine up to what redshift they remain useful for statistical studies. The visual inspection is performed by examining each density map for the presence of coherent, spatially extended structures across multiple kernel scales and the smoothness of the density field. Even though the number of galaxies decreases at higher redshifts, the maps still display structures and smooth variations in density. At $z > 7$, the density maps either become flat or exhibit sharp, nonsmooth variations. While the contrast between dense and sparse regions is lower than at lower redshifts, the density maps remain usable up to $z \sim 7$ for statistical studies of how galaxy properties such as mass and SFR relate to environment.

Based on this, we adopt $z \sim 7$ as the maximum redshift for reliable density measurements for the purpose of our study, which focuses on the connection between environment and galaxy properties such as stellar mass and SFR.

5. Discussion

Our density construction based on COSMOS-Web provides a new perspective on how galaxy environments evolve across cosmic time. In this section, we first discuss how COSMOS-Web improves measurements in the cosmic web compared to COSMOS2020. We then investigate how the density contrast correlates with galaxy properties.

5.1. LSS with COSMOS-Web Compared to COSMOS2020

Accurately measuring the cosmic environment of galaxies relies heavily on the quality of photometric redshift estimates.

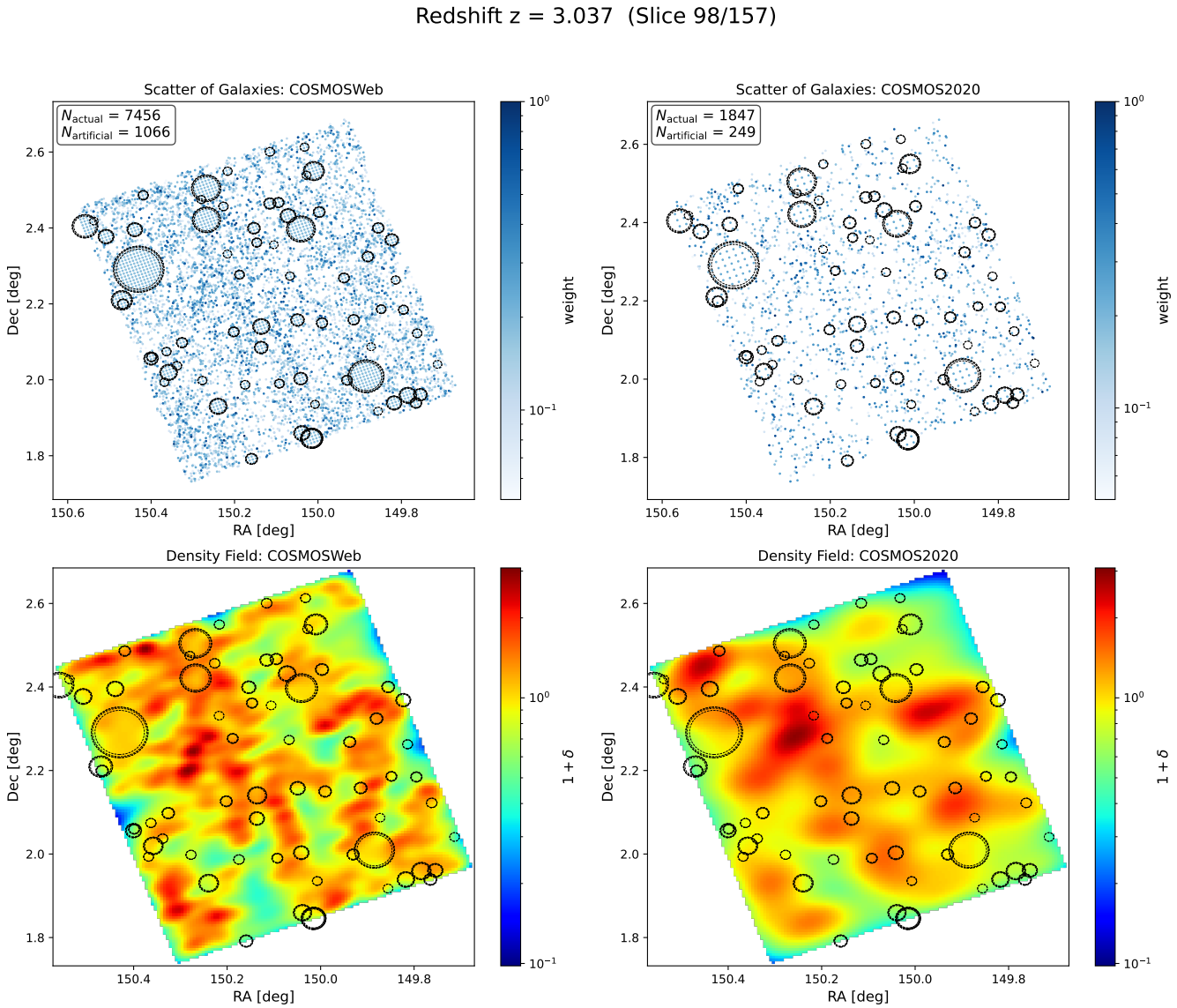

Figure 8. Comparison of density field reconstructions in a slice at $z \sim 3.0$, using COSMOS-Web (left) and COSMOS2020 (right). Top panels: galaxy distributions in each slice, with points colored by their weights. Bottom panels: corresponding overdensity maps, colored by $\log(1 + \delta)$. The COSMOS-Web reconstruction recovers smoother and more coherent LSSs, due to its deeper completeness, higher source density, and improved photometric redshift precision, whereas the COSMOS2020 map appears sparser, more diffuse, and missing some details in the structures. The circles indicate the HSC masked regions.

Since our density fields are constructed using the redshift probability distributions of galaxies, more precise redshifts lead to more localized and reliable weight assignments within each slice. With COSMOS-Web, the precision of the photometric redshifts has improved compared to COSMOS2020, with COSMOS-Web galaxies having a lower $\sigma_{\rm NMAD}$ and reduced outlier fractions compared to COSMOS2020. These improvements are more significant for fainter galaxies (M. Shuntov et al. 2025a). In COSMOS2020, broader and less accurate redshift PDFs cause galaxy weights to spread to more slices, diluting any potential structure. In COSMOS-Web, narrower PDFs allow galaxies to contribute more accurately to the correct slice, resulting in cleaner and better-resolved density maps.

In addition to better redshift precision, COSMOS-Web includes more galaxies than COSMOS2020 within the same area, especially at fainter magnitudes. Given the near-infrared selection criterion and deeper photometric data of COSMOS-Web, it contains more galaxies, especially at fainter limits, and therefore provides a more complete sample at all redshifts. The lower number of galaxies in COSMOS2020 can lead to gaps in coverage and more variation in the density maps, especially at higher redshifts. We limit the COSMOS2020 sample to the COSMOS-Web area, therefore the maps are directly comparable. These differences are visible in Figure 8, which compares one redshift slice ($z \sim 3$) between the two catalogs. In the top panels, the distribution of galaxies shows that COSMOS-Web includes far more galaxies in the slice. The bottom panel shows the density maps for both catalogs. The COSMOS2020 map appears smoother and more diffuse, with some structures entirely missed. This comparison illustrates how increased galaxy counts and improved redshifts together allow the detection of LSS features that were not revealed before.

The comparison between the COSMOS-Web and COSMOS2020 density contrasts up to $z \sim 4$ reveals that the two catalogs differ systematically in how they represent both

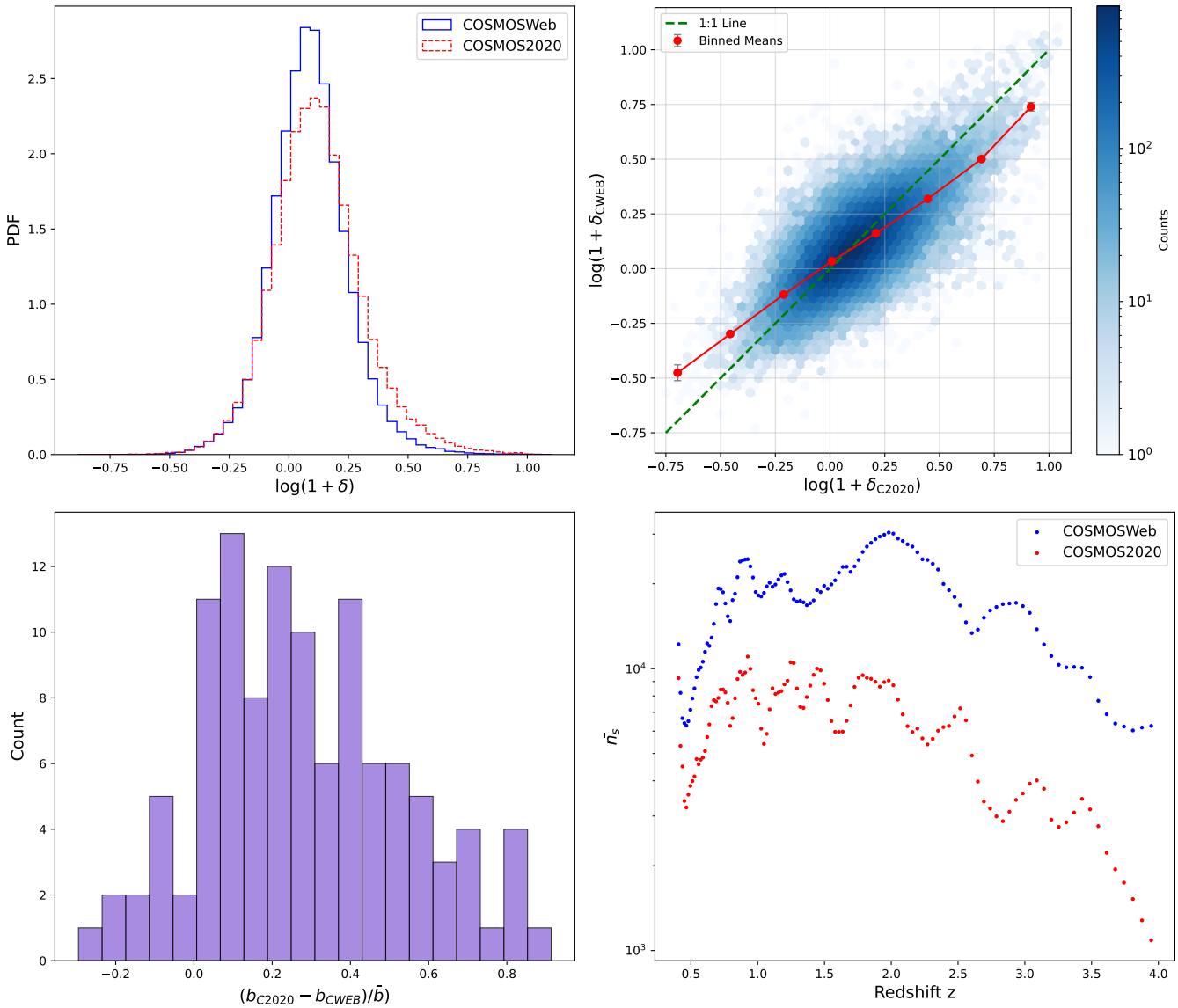

Figure 9. Comparison of density field diagnostics between COSMOS-Web and COSMOS2020 up to a redshift of 4. Top left: PDF of $\log(1+\delta)$ for both surveys. Top right: galaxy-by-galaxy comparison of $\log(1+\delta_{\rm CWEB})$ and $\log(1+\delta_{\rm C2020})$ with binned means and 1:1 line (where the two quantities are equal). Bottom left: relative difference in the global bandwidth b_s for each redshift slice, normalized by their means. Bottom right: mean surface number density n_s per slice for COSMOS-Web and COSMOS2020.

overdense and underdense regions. Figure 9 summarizes the key diagnostics:

1. The top left panel shows the PDFs of $\log(1+\delta)$ for all galaxies that are crossmatched between the two surveys. COSMOS2020 exhibits a broader high-density tail, indicating more regions assigned very large overdensities. COSMOS-Web, while recovering the same LSSs, produces a more concentrated distribution with fewer extreme peaks. This suggests that COSMOS2020 is prone to inflating the contrast in high-density regions.
2. The top right panel compares $\log(1+\delta_{\rm CWEB})$ and $\log(1+\delta_{\rm C2020})$ for individual galaxies crossmatched between catalogs, with binned means overplotted. The relation follows the 1:1 line at intermediate densities but diverges at both ends. In high-density regions, the density contrast in COSMOS2020 systematically exceeds COSMOS-Web, while in low-density regions, it produces less negative contrasts, making voids appear shallower compared to COSMOS-Web. The result remains the same with different binning. The difference is caused by the differences in sampling, KDE smoothing (b_s), and density normalization ($\bar{n}_s$) between the catalogs.
3. The bottom left panel shows the relative difference in the optimal global bandwidth b between COSMOS2020 and COSMOS-Web for each slice, normalized by the slice mean $\bar{b}$. In almost all slices, $b_{\rm C2020}$ is larger, reflecting the sparser sampling in COSMOS2020. With fewer tracers, the LCV algorithm selects a broader smoothing scale, which spreads the galaxy signal into nearby voids and makes the density contrast less negative in those regions. COSMOS-Web, with denser sampling, adopts smaller b values that preserve the amplitude of the underdensities and finer features in structures. In overdense regions, the larger b in COSMOS2020 also spreads the clustered galaxy signal into surrounding cells, inflating peak contrasts.

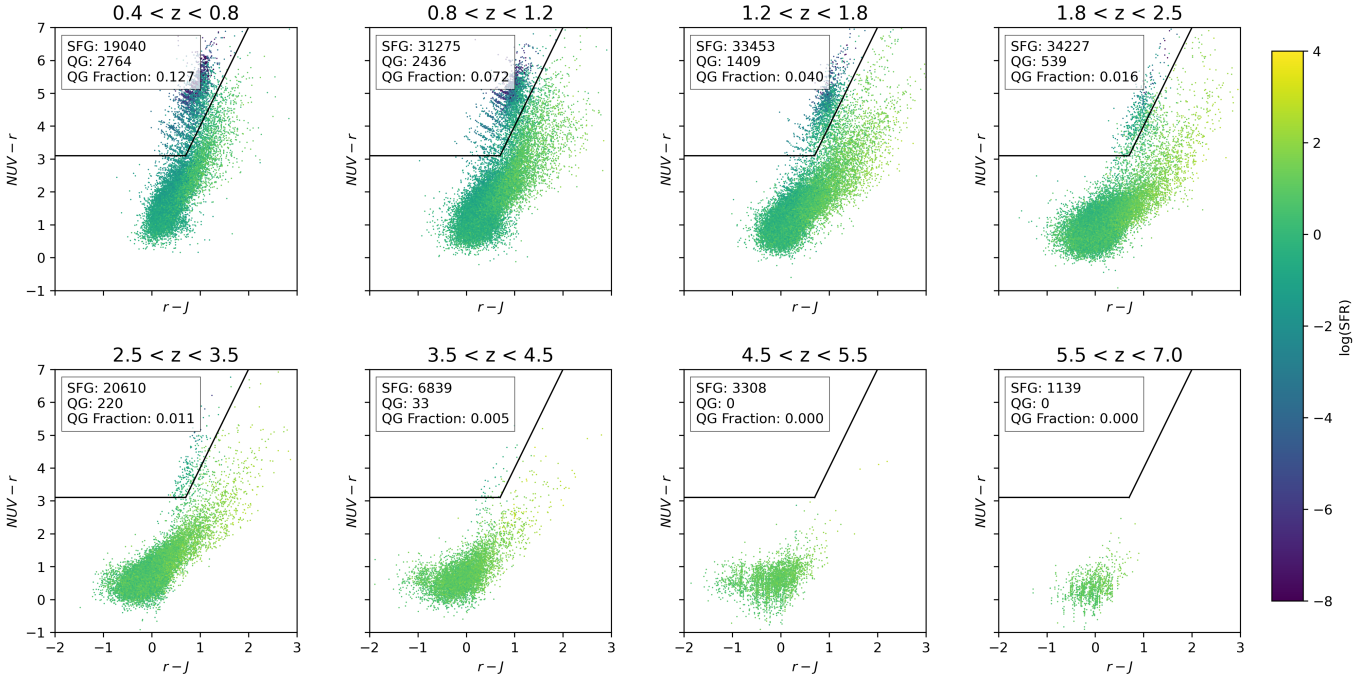

Figure 10. Rest-frame color–color diagrams ($NUV - r$ versus $r - J$) in different redshift bins, used to separate SFGs from QGs. The color scale shows log(SFR). Each panel shows one redshift interval, with the black lines indicating the quiescent and star-forming selection criteria. The number of SFGs, QGs, and the quiescent fraction are reported in each bin.

4. Finally, the bottom right panel shows the mean number density $\bar{n}_s$ of galaxies per slice for the two surveys. COSMOS-Web has a consistently higher $\bar{n}_s$ across all redshifts, owing to its deeper flux limit and inclusion of faint galaxies. Since δ is defined relative to $\bar{\sigma}$, a higher mean surface density reduces the measured $(1 + \delta)$ for any fixed absolute density σ. This normalization effect compresses the dynamic range of $\delta_{\rm CWEB}$ compared to $\delta_{\rm C2020}$, even when both are sampling the same underlying matter peaks. Also, the mean number density drops down significantly at higher redshifts in the COSMOS2020 sample ($z > 3.5$).

All these diagnostics show that COSMOS2020 tends to overestimate densities in the most overdense environments and to underestimate the depths of underdense regions. This result demonstrates how improvements in photometric redshift precision and sample completeness impact the reconstruction of the large-scale density field and, consequently, the environmental metrics used for galaxy evolution studies. COSMOS-Web, with its higher completeness, smaller smoothing bandwidths, and lower tracer bias, produces a more accurate mapping of the LSS, even if the resulting δ field has a smaller dynamic range. This shift has direct implications for environmental studies. Trends measured with $\delta_{\rm C2020}$ may appear artificially steep in the highest-density bins and artificially shallow in the lowest-density bins, whereas $\delta_{\rm CWEB}$ better preserves the true relative contrast across environments.

5.2. Evolution of Mass with Large-Scale Environment Density

Mass is one of the most fundamental properties that reveals the evolution of galaxies. Understanding the environmental dependence of stellar mass as a function of cosmic epoch would give us insight into the role of LSS in driving the evolution of galaxies. Many previous studies have shown that, at low redshift, more massive galaxies reside in denser regions, though the strength and statistical significance tend to decline with increasing redshift (B. Darvish et al. 2015; N. Chartab et al. 2020; B. C. Lemaux et al. 2022; S. Taamoli et al. 2024b). To better understand environmental effects on galaxy evolution, we analyze three samples: one with all galaxies (star-forming and quiescent), one with only star-forming galaxies (SFGs), and one with only quiescent galaxies (QGs). We identify QGs in each bin using the rest-frame color–color diagram ($NUV - r$ versus $r - J$) and the classification criteria from O. Ilbert et al. (2013). Galaxies with $NUV - r > 3.1$ and $NUV - r > 3(r - J) + 1$ are classified as quiescent. Figure 10 shows the distribution of galaxies in the color–color plane, showing the QG and SFG populations, their SFRs, and the corresponding quiescent fraction. We do not impose a threshold for SFR or sSFR when selecting our QG sample, as doing so could introduce biases into the subsequent analysis of SFR and sSFR versus density. The QG fraction decreases as we look at higher redshift, which is expected from the growth of the quiescent population over cosmic time (O. Ilbert et al. 2013; A. Muzzin et al. 2013). Also at redshifts $z > 2.5$, the QG sample is too limited for a robust physical interpretation.

In Figure 11, we show the distribution of stellar mass as a function of environmental overdensity in eight redshift bins, from $z = 0.4$ to $z = 7$. At lower redshifts, a large number of galaxies are present across a wide range of environments. While most galaxies lie in the low-mass regime ($\log(M_*/M_\odot) \sim 8.5$–$10$), there is a population of higher-mass galaxies extending toward higher overdensities. As redshift increases, the distribution narrows both in stellar mass and in environmental density.

To quantify the mass–density relation, we show the average stellar mass as a function of overdensity in Figure 12. The left panel shows the results for the full galaxy population, the middle panel shows SFGs only, and the right panel shows

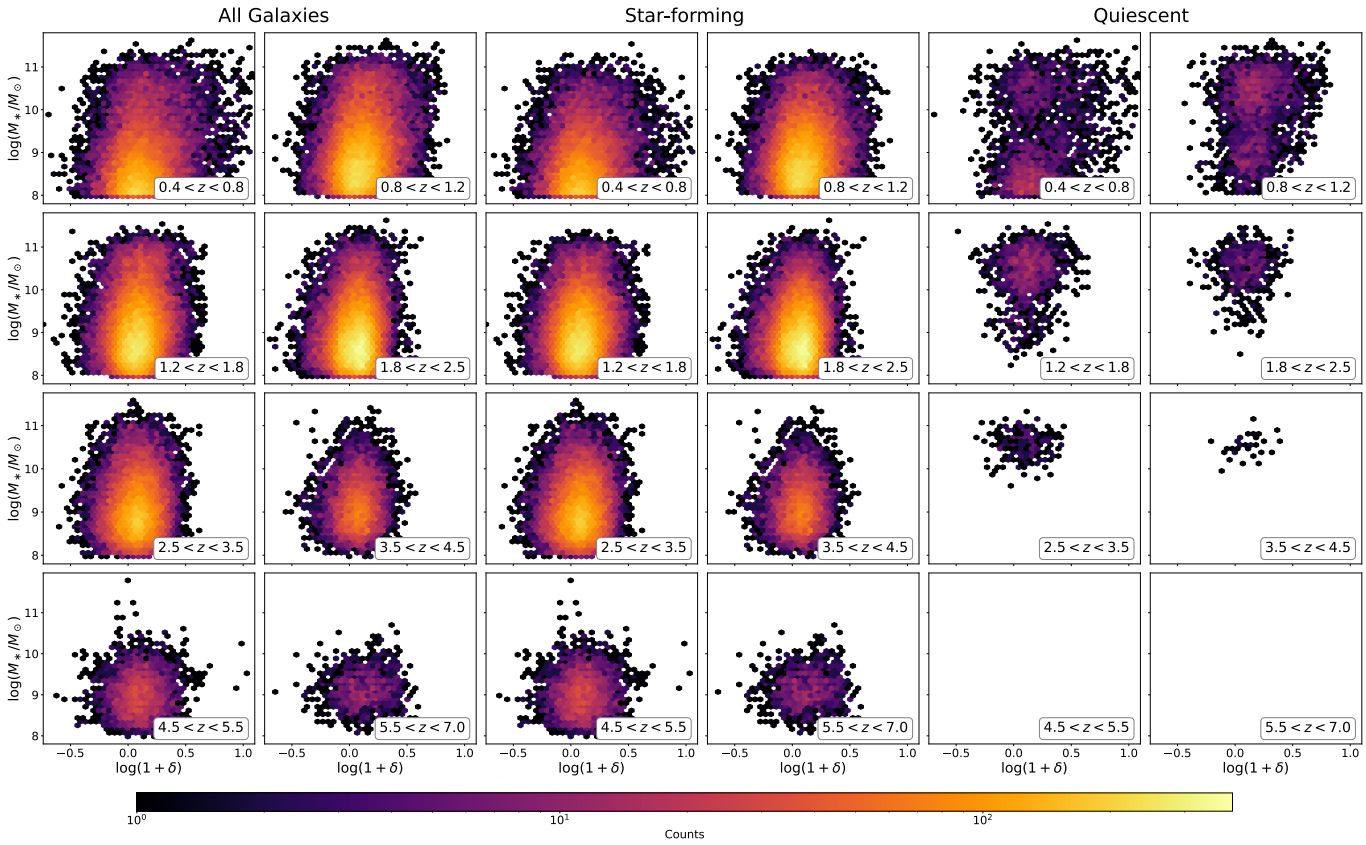

Figure 11. Stellar mass as a function of environmental overdensity in COSMOS-Web. Each row shows a different redshift bin, increasing from top to bottom, and each column corresponds to a galaxy population: all galaxies (left), SFGs (middle), and QGs (right). Points are colored by number counts. The distribution narrows with increasing redshift.

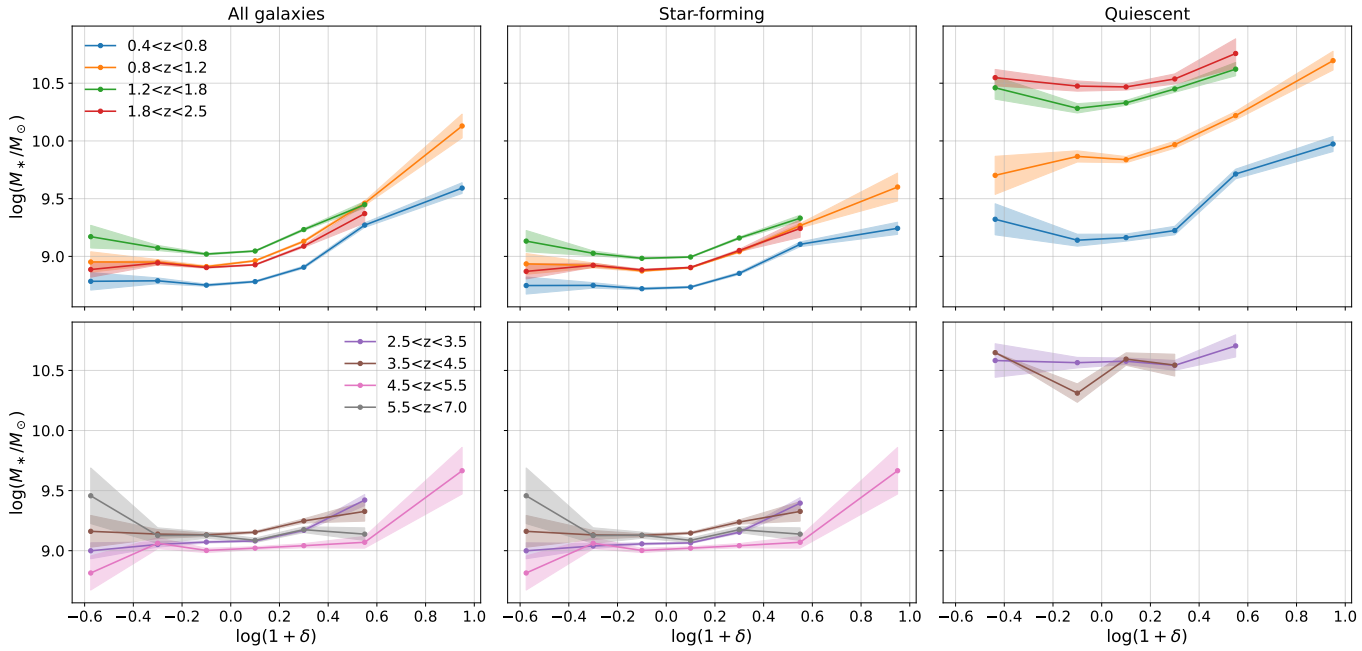

Figure 12. Average stellar mass as a function of environmental overdensity in COSMOS-Web. The columns show all galaxies (left), SFGs (middle), and QGs (right). The top row corresponds to redshift bins in the range $0.4 < z < 2.5$ and the bottom row to $2.5 < z < 7.0$. At $z \lesssim 2.5$, stellar mass increases with overdensity for all galaxies—most strongly for quiescent systems—while the trend for SFGs is weaker. At higher redshifts, the correlation is only visible in the most overdense regions. The shaded regions indicate the standard error on the mean in each overdensity bin.

QGs. In all cases, we observe a general trend, where stellar mass increases with overdensity, although the trend is weaker in the SFG sample. The nature of this positive correlation between mass and density evolves with time. At lower redshifts ($z < 2.5$), the correlation is strong and evident even at moderate overdensities. Galaxies in overdense regions with

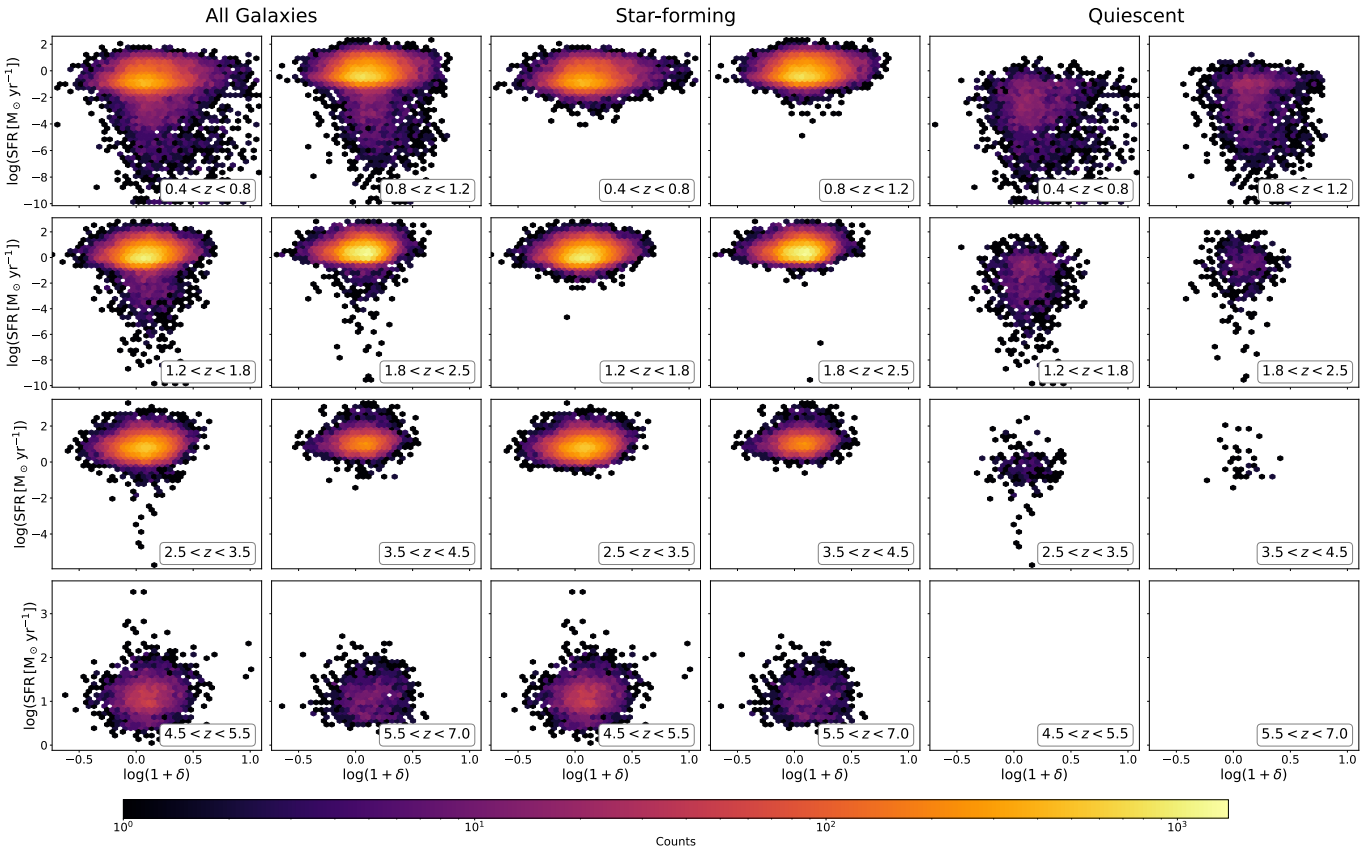

Figure 13. SFR as a function of environmental overdensity in COSMOS-Web. Each row corresponds to a different redshift bin, increasing from top to bottom, and each column corresponds to a galaxy population: all galaxies (left), SFGs (middle), and QGs (right). Points are colored by number counts. The distribution becomes narrower with increasing redshift, and the quiescent sample is sparse at $z \gtrsim 2.5$.

$\log(1+\delta) \gtrsim 0.3$ tend to be about 0.3–0.6 dex (a factor of 2–4) more massive than those in average or underdense environments. This is consistent with expectations from hierarchical structure formation, where overdense environments host earlier and more rapid mass assembly. In the star-forming sample, the trend is still present but weaker, and the average mass is lower compared to QGs. This shows that massive galaxies in dense environments are more likely to be quiescent, which is a consequence of merging at later epochs.

At higher redshifts ($z > 2.5$), the trend persists but becomes limited to the highest-density environments and is dominated by SFGs. The stellar-mass–density correlation is no longer present across all environments, only at the upper end of the overdensity distribution (e.g., $\log(1+\delta) \gtrsim 0.4$), where the mass difference remains small ($\lesssim$0.2 dex). This suggests that only the most extreme peaks of the matter density field, such as protoclusters, host galaxies that have grown significantly in mass by those epochs. The reduced statistical range of environments at early times may also contribute to the flattening of the trend in the low- and intermediate-density regions. This implies that the underlying physical processes—such as biased halo formation, gas accretion, and merging—are in place from early times, but their influence is confined to dense regions in the early Universe. As cosmic structures grow and evolve, these processes extend to more typical environments, producing a smoother and more extended mass–density correlation at later times.

Our mass–environment trends are consistent with other studies. In the CANDELS field, N. Chartab et al. (2020) found that more massive galaxies preferentially reside in overdense regions, but the strength of the correlation declines toward higher redshifts. They also found that the correlation is stronger with QGs and weaker for SFGs. With the COSMOS2020 data, S. Taamoli et al. (2024b) reported a similar positive mass–density relation up to $z \sim 4$, with a gradual weakening at earlier epochs. They also note that at $z > 2$, where the peak of star formation activity takes place, only the most extreme overdensities host galaxies that have already assembled significant stellar mass, consistent with our observation that the correlation at early times is limited to the upper tail of the density distribution. Compared to other works, COSMOS-Web's depth provides better mass completeness at high redshift, allowing us to trace the mass–density relation into regimes (low-mass, high-z) that were inaccessible in previous surveys. This combination of completeness and more accurate environment detection strengthens the statistical significance of the trends observed for COSMOS-Web, particularly at higher redshifts.

The positive correlation between the stellar mass and environment at low redshift can be explained within the hierarchical structure formation framework, where the highest peaks in the density field collapse earlier, leading to accelerated mass assembly (S. D. M. White & M. J. Rees 1978; H. J. Mo & S. D. M. White 1996). In these regions, the higher frequency of galaxy mergers (O. Fakhouri et al. 2010; J. M. Lotz et al. 2011; F. Giddings et al. 2026) contributes to the buildup of massive systems, particularly QGs at later times. Once dark matter halos reach $\sim 10^{12}\,M_{\odot}$,

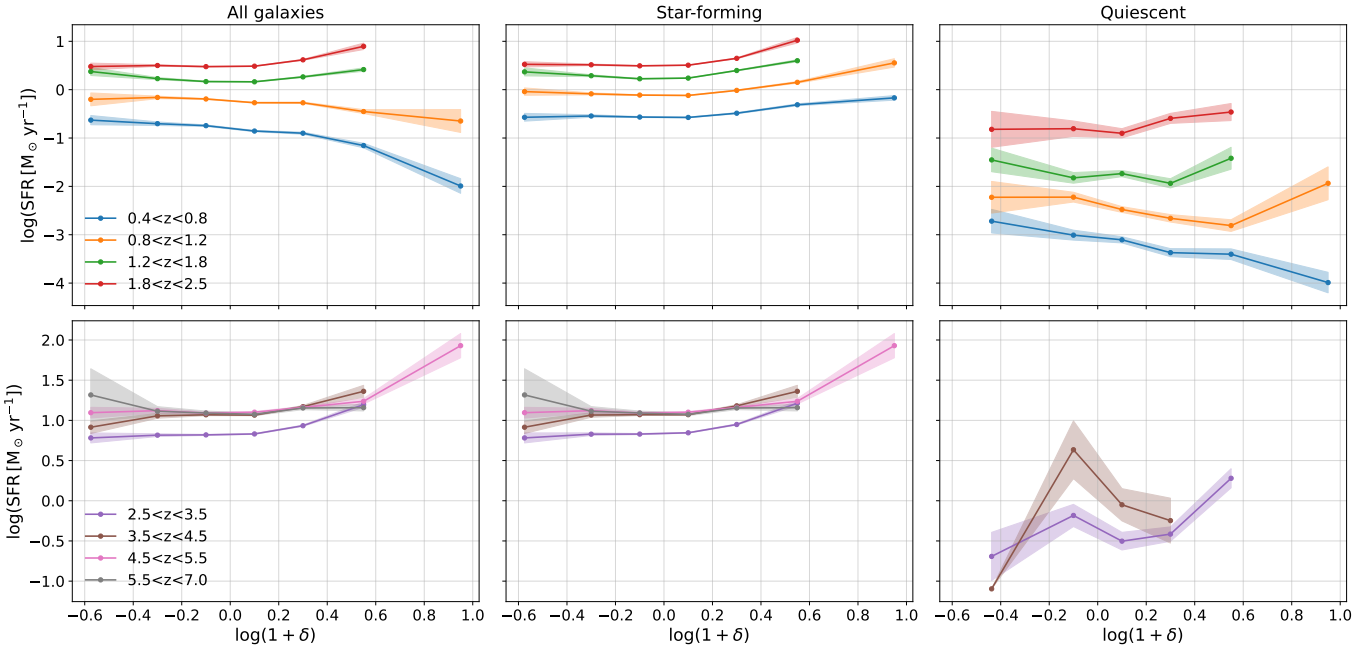

Figure 14. Average SFR as a function of environmental overdensity in COSMOS-Web. The columns show all galaxies (left), SFGs (middle), and QGs (right). The top row corresponds to redshift bins in the range $0.4 < z < 2.5$ and the bottom row to $2.5 < z < 7.0$. For the full population, SFR decreases with overdensity at $z \lesssim 1.2$, driven mainly by the higher quiescent fraction in dense regions. SFGs instead show a mild increase of SFR with density up to $z \sim 5.5$, while QGs display a negative trend at $z \lesssim 1.2$ and a mild increase at the highest densities at $z > 1.2$. Standard uncertainties are indicated with the shaded regions.

infalling gas is shock heated and the accretion mode changes from cold to hot (Y. Birnboim & A. Dekel 2003; A. Dekel & Y. Birnboim 2006), reducing the supply of fresh gas. Combined with feedback from active galactic nuclei (D. J. Croton et al. 2006; A. C. Fabian 2012), this leads to quenching while preserving high stellar mass. A significant fraction of galaxies are also affected by preprocessing in group environments before entering clusters, where tidal interactions and mergers increase their stellar mass (A. R. Wetzel et al. 2013). At higher redshift, dense filaments feeding protoclusters can sustain high cold-gas accretion rates (D. Kereš et al. 2005; A. Dekel et al. 2009; E. Daddi et al. 2022). This allows galaxies in the most overdense regions to assemble large stellar masses earlier than those in lower-density environments, consistent with our $z > 2.5$ results.

The mass–density relation can also be influenced by star formation activity and the efficiency of mass and environment quenching processes. Since both SFR and quenching affect the rate at which galaxies build up stellar mass, differences in these processes with density can shape parts of the observed trends. These connections are explored further in Sections 5.3 and 5.4.

5.3. Evolution of SFR and sSFR with Large-scale Environment Density

Studying how the SFR and sSFR vary with LSS density helps us understand whether galaxies form stars differently depending on their surrounding environment. Figure 13 shows the distribution of SFR as a function of overdensity across redshift bins for our three samples. For the full sample at low redshift ($z < 1.8$), there is a clear tendency for galaxies with higher SFR to occupy lower-density regions, while high-density environments host fewer galaxies with strong SFR. This trend is more pronounced at lower redshift and gradually weakens with increasing redshift. The star-forming sample exhibits a much flatter distribution across environments in the same redshift range, which suggest environments have a mild effect on the SFR of active SFGs. Meanwhile, the quiescent population shows a negative correlation with density at $z < 0.8$. This correlation diminishes at higher redshifts. Therefore, the trend seen in the full sample is primarily driven by the growing quiescent population in overdense regions at lower redshifts, which suppresses the average SFR in the total sample.

Figure 14 shows the average trend of SFR with LSS density. For the full sample (left panels), the trend is negative at $z < 1.2$, with SFR decreasing steadily toward higher densities. In the $1.2 < z < 1.8$ bin, this decline flattens, and by $z > 1.8$ the trend reverses and galaxies in overdense environments tend to have higher SFRs than those in underdense regions. Breaking the sample into galaxy types reveals the cause of the evolution in the full-sample trend. In the star-forming sample (middle panels), SFR shows a mild positive correlation with density up to $z < 5.5$, with galaxies in denser regions forming stars at rates up to 0.5 dex higher, with the trend diminishing in the early epoch. In contrast, the quiescent population (right panels) displays a negative environmental dependence for $z < 0.8$. In the $0.8 < z < 1.2$ epoch, SFR decreases by about 1 dex with density up to $\log(1 + \delta) < 0.6$, but SFR increases again at the highest-density regions. This upturn in SFR is likely due to a greater gas reservoir in the densest region. Also, these dense environments may host recently quenched galaxies with residual star formation or galaxies with brief rejuvenation due to minor mergers or tidal interactions (V. Wild et al. 2016; M. J. Rutkowski et al. 2025). Moreover, there is no clear evolution for QGs at higher redshifts. So, the decline in SFR with density for the full sample is just coming from QGs having lower SFR values in general.

Figure 15 shows how sSFR changes with overdensity for different redshift bins and galaxy types. For the star-forming

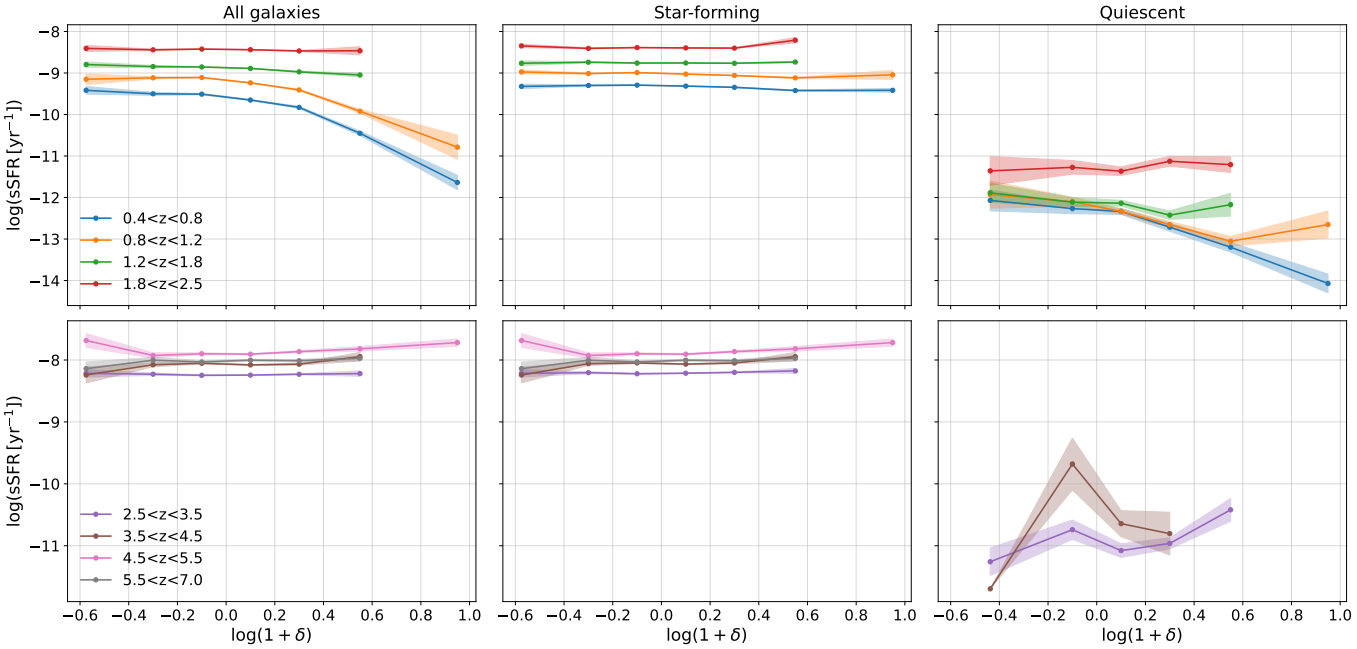

Figure 15. Average sSFR as a function of environmental overdensity in COSMOS-Web. The columns show all galaxies (left), SFGs (middle), and QGs (right). The top row corresponds to redshift bins in the range $0.4 < z < 2.5$ and the bottom row to $2.5 < z < 5.0$. At low redshift, sSFR declines in overdense regions due to QGs, while SFGs maintain nearly flat sSFR across environments. At higher redshifts, the dependence on environment largely disappears for both populations. Standard uncertainties are shown with the shaded areas.

sample, the sSFR stays nearly constant across all environments and redshifts. This is expected, since both the SFR and stellar mass of these galaxies increase with density, keeping the ratio roughly the same. Similar flat trends have been reported in other studies, showing that the environment does not have a significant effect on sSFR for SFGs (N. Scoville et al. 2013; B. Darvish et al. 2016; S. Taamoli et al. 2024a).

At low redshifts ($z < 1.2$), the sSFR for QGs decreases with increasing density, which is consistent with a drop in SFR and an increase in mass. This trend supports the idea that environmental quenching—such as gas stripping or starvation—suppresses residual star formation in dense environments (Y.-j. Peng et al. 2010; J. Woo et al. 2013). In the $0.8 < z < 1.2$ bin, the sSFR increases again at the highest densities. This may be due to recently quenched galaxies with low-level star formation or temporary rejuvenation events triggered by interactions or mergers (V. Wild et al. 2016; M. J. Rutkowski et al. 2025). Above $z > 1.2$, there is no clear trend, suggesting that the effect of environment on sSFR becomes weaker at early times (S. Taamoli et al. 2024a, 2024b). In the full sample, we see a negative trend for sSFR and overdensities up to $z < 1.2$, but it is largely caused by the evolution of QGs.

Our findings broadly agree with recent studies. At low redshift ($z \lesssim 1.2$), our negative correlation between SFR and overdensity is consistent with the results of N. Chartab et al. (2020) and S. Taamoli et al. (2024a), who both report significant suppression of SFR in denser regions out to $z \sim 1.1$. The flattening we observe at $1.2 < z < 1.8$ matches the transitional regime identified by S. Taamoli et al. (2024a), where the correlation weakens and becomes statistically insignificant. Beyond $z \gtrsim 1.8$, we find a clear reversal in correlations. Galaxies in overdense regions exhibit enhanced SFR, which is in agreement with B. C. Lemaux et al. (2022) and S. Taamoli et al. (2024a), who both report a monotonic increase in SFR (and sSFR) with density at $z > 2$. However, the amplitude of our reversal appears somewhat smaller than in B. C. Lemaux et al. (2022), who find up to an order-of-magnitude enhancement between the lowest and highest densities. This may reflect differences in sample selection or the range of probed environments. Compared to N. Chartab et al. (2020), who report no statistically significant reversal up to $z \sim 3.5$, our detection likely benefits from deeper near-infrared data and improved photometric redshift precision in COSMOS-Web, and larger sky-area coverage compared to CANDELS, enabling more reliable density estimation at higher redshifts.

The negative correlation between SFR and LSS density at low redshifts ($z \lesssim 1.2$) is consistent with environmentally driven quenching processes that are more effective in dense regions (S. Taamoli et al. 2024b). We will discuss how quenching efficiencies can replicate SFR trends with density in Section 5.4. Mechanisms such as ram pressure stripping can rapidly remove the cold-gas reservoir from galaxies moving through cluster environments (J. E. Gunn & J. R. Gott 1972; A. Boselli & G. Gavazzi 2006). This process can shut down star formation on short timescales ($\sim$1 Gyr). Strangulation or starvation (B. Moore et al. 1999; Y. Peng et al. 2015) suppress star formation more gradually, by cutting off the supply of fresh cold gas from the cosmic web, leading to quenching over $\sim 1-3$ Gyr. Moreover, tidal harassment from repeated high-speed encounters can both strip gas and dynamically heat the stellar disk, indirectly reducing star formation efficiency (B. Moore et al. 1996). In addition, AGN feedback—which is more prevalent in massive galaxies in dense environments—can heat or expel the interstellar medium, thereby suppressing star formation and reinforcing quenching in these regions (A. C. Fabian 2012; B. A. Terrazas et al. 2020).

At higher redshifts ($z \gtrsim 1.8$), the reversal of the SFR–density relation suggests that dense environments may instead enhance star formation activity. One of the contributing factors for this reversal is SFGs dominating the sample at higher

Table 2
Correlation Coefficients versus Density (Binned by $\log(1+\delta)$)

Redshift Range	N	$\log(M_{10\%}/M_{\odot})$	Correlation Mass versus Density			Correlation SFR versus Density			Correlation sSFR versus Density		
			All	SFG	QG	All	SFG	QG	All	SFG	QG
$0.4 < z < 0.8$	21,535	8.11	0.89	0.89	0.81	−0.90	0.90	−0.98	−0.90	−0.84	−0.96
$0.8 < z < 1.2$	33,075	8.22	0.86	0.85	0.90	−0.98	0.80	0.13	−0.92	−0.71	−0.72
$1.2 < z < 1.8$	34,254	8.29	0.65	0.58	0.49	0.12	0.58	−0.15	−0.97	0.31	−0.86
$1.8 < z < 2.5$	33,990	8.24	0.84	0.87	0.81	0.82	0.76	0.70	0.51	0.55	0.07
$2.5 < z < 3.5$	20,163	8.37	0.82	0.80	0.33	0.81	0.82	0.74	0.48	0.85	0.74
$3.5 < z < 4.5$	6473	8.49	0.71	0.69	−0.13	0.90	0.90	0.32	0.86	0.85	0.27
$4.5 < z < 5.5$	3243	8.39	0.79	0.79	⋯	0.74	0.74	⋯	0.26	0.26	⋯
$5.5 < z < 7.0$	1121	8.58	−0.70	−0.70	⋯	−0.58	−0.58	⋯	0.83	0.83	⋯

redshifts. Another key factor behind this is galaxies at early times containing a much larger reservoir of cold gas. L. J. Tacconi et al. (2010) found that the cold gas made up roughly 44% of the baryonic mass in galaxies at $z \sim 2.3$, and about 34% at $z \sim 1.2$, which is higher than in the local Universe. These large gas supplies provided abundant fuel for star formation. Another is the supply of cold gas from LSS filaments feeding protoclusters, which can sustain high SFRs (A. Dekel et al. 2009). Dense environments at these epochs also tend to have higher rates of galaxy–galaxy interactions and mergers, which can sometimes trigger starbursts (G. F. Snyder et al. 2017; E. Ventou et al. 2019; F. Giddings et al. 2026). Moreover, the rapidly evolving gravitational potential in assembling structures can tidally compress gas, further inducing bursts of star formation (K. Bekki 1999). Also, the cosmic web is not mature enough to quench galaxies as efficiently as at lower redshifts (S. Taamoli et al. 2024b). QGs are responsible for the SFR–density trend in general at low redshifts. Therefore, with galaxies being mostly starburst at higher redshifts, the SFR–density trend becomes dominated by SFGs, which have a positive correlation with density.

The nearly flat sSFR–density relation for SFGs across most redshifts implies that the environmental dependence of their SFR is closely coupled to their stellar-mass growth. In denser regions, both SFR and M_* increase in parallel, keeping sSFR roughly constant. This is consistent with scenarios where the same processes that enhance gas supply—e.g., cold-gas accretion along filaments and merger-driven inflows—also drive faster stellar-mass assembly (A. Dekel et al. 2009; J. S. Speagle et al. 2014; R. Genzel et al. 2015). For QGs, the negative sSFR–density trend at low z reflects both suppressed SFR and higher masses in denser regions, consistent with environmental quenching acting more strongly where galaxy interactions are prevalent (N. Chartab et al. 2020; S. Taamoli et al. 2024b). Since sSFR measures the relative growth rate of stellar mass, its environmental dependence directly links the SFR trends discussed here to the mass–density relation in Section 5.2. These variations in sSFR indicate differences in how efficiently QGs and SFGs build mass in different environments, helping to explain part of the mass–environment correlation. We explore this relation in Section 5.4, to quantify the effects of mass and environment.

To assess whether the enhanced stellar mass of galaxies in overdense regions can be explained by secular star formation, we compare the median stellar mass and SFR of SFGs in the lowest and highest quartiles of the overdensity distribution within each redshift bin. For $z > 2$, the stellar-mass excess $\Delta \log M^{\star} \simeq 0.10$ to 0.11 dex matches the SFR enhancement $\Delta \log \mathrm{SFR} \simeq 0.10$ to 0.11 dex, and the corresponding sSFR offsets are consistent with zero $\Delta \log \mathrm{sSFR} \simeq 0.00$ to 0.03 dex. This indicates that SFGs in dense environments grow at similar mass-normalized rates but with higher absolute SFR, showing that in situ star formation can account for the environmental mass dependence at early times. For $z < 1$, the stellar-mass excess remains significant $\Delta \log M^{\star} \simeq 0.23$ to 0.25 dex, while the SFR enhancement is weaker $\Delta \log \mathrm{SFR} \simeq 0.16$ dex, and the sSFR is suppressed $\Delta \log \mathrm{sSFR} \simeq -0.06$ dex. In this regime, secular star formation alone cannot build the observed mass excess within the available cosmic time, so additional processes —such as gas-rich mergers at earlier times and dry mergers at later times—likely contribute to the accelerated mass assembly in dense environments prior to quenching.

Table 2 presents Pearson correlation coefficients between $\log(1+\delta)$ and stellar mass, SFR, and sSFR. In each redshift interval, galaxies are binned by $\log(1+\delta)$ using the same density bins as in Figures 12, 14, and 15. For each density bin and for each sample (All, SFGs, and QGs), we compute the mean of the corresponding quantity, and we then evaluate the correlation between those binned means and $\log(1+\delta)$. The table lists the coefficients, together with the sample size N and the 10th percentile stellar mass $\log(M_{10\%}/M_{\odot})$. The results are consistent with the trends shown in Figures 12, 14, and 15. The highest-redshift bin ($5.5 < z < 7.0$) has a small sample size, and the scatter plots of physical parameters (e.g., stellar mass, SFR, and sSFR) do not show strong correlations with density. Therefore, the correlation coefficients should be interpreted with caution, even though the p-values are small ($P < 0.01$) for this bin.

5.4. The Roles of Environment and Mass in Galaxy Quenching

The trends in QG physical parameters with overdensity presented in the previous subsections suggest that both stellar mass and large-scale environment play a role in shutting down star formation. To examine how galaxies are distributed across different environments, we divide the density field into three regimes, based on their overdensity. Galaxies are sorted by their density contrast, and the P_{25} and P_{75} percentiles are computed, and we find low-, medium-, and high-density regions in each redshift bin:

1. Low density: $\delta \leqslant P_{25}$;
2. Medium density: $P_{25} < \delta \leqslant P_{75}$; and
3. High density: $\delta > P_{75}$.

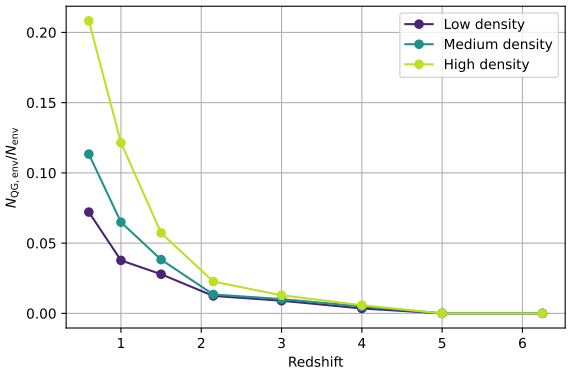

Figure 16. Quiescent fraction as a function of redshift in different environments. The curves show $f_{QG,env} = N_{QG,env}/N_{env}$ measured within each redshift bin for low-density ($\delta \leqslant P_{25}$), medium-density ($P_{25} < \delta \leqslant P_{75}$), and high-density ($\delta \geqslant P_{75}$) regions. $N_{QG,env}$ is the number of QGs in a given environment, and N_{env} is the number of galaxies in that environment. Density percentiles (P_{25}, P_{75}) are computed separately in each redshift bin from the overdensity distribution. The fraction of QGs in dense environments is higher at all redshifts.

As shown in Figure 16, the quiescent fraction increases with time, and at later epochs high-density regions have a higher quiescent fraction compared to other environments. However, to disentangle these effects, we follow the framework introduced by Y.-j. Peng et al. (2010), where galaxy quenching is described as the combination of two independent processes: mass quenching and environmental quenching. In this picture, the probability that a galaxy is quenched can be factorized into contributions from each process (Y.-j. Peng et al. 2010, 2012; B. Darvish et al. 2016; L. Kawinwanichakij et al. 2017; N. Chartab et al. 2020; B. C. Lemaux et al. 2022; S. Taamoli et al. 2024b).

Mass quenching is generally associated with internal processes that scale with stellar mass or halo potential, such as virial shock heating in massive halos (A. Dekel & Y. Birnboim 2006), feedback from active galactic nuclei (D. J. Croton et al. 2006; A. C. Fabian 2012), morphological quenching (M. Martig et al. 2009), or the exhaustion of cold-gas reservoirs. Environmental quenching is instead linked to processes induced by the surrounding LSS, including ram pressure stripping (J. E. Gunn & J. R. Gott 1972), harassment and tidal interactions, strangulation, and the suppression of cold-gas accretion in dense regions (B. Moore et al. 1996; A. Dekel et al. 2009).

To quantify these processes, we measure the quenching efficiencies following Y.-j. Peng et al. (2010), N. Chartab et al. (2020), and S. Taamoli et al. (2024b). The environmental quenching efficiency is defined as

$$\epsilon_{env}(M_\star, z) = 1 - \frac{f_{SF}(\delta \geqslant P_{75},\ M_\star,\ z)}{f_{SF}(\delta \leqslant P_{25},\ M_\star,\ z)}, \tag{11}$$

where $f_{SF} = 1 - f_{QG}$ is the star-forming fraction. This measures the fraction of galaxies that would be star-forming in low-density regions but are quenched in denser environments.

Similarly, the mass-quenching efficiency is defined as

$$\epsilon_{mass}(M_\star, z|\delta \geqslant P_{75}) = 1 - \frac{f_{SF}(M_\star,\ \delta \geqslant P_{75},\ z)}{f_{SF}(M_0,\ \delta \geqslant P_{75},\ z)}, \tag{12}$$

where M_0 is the lowest-stellar-mass bin in the same redshift slice. This measures the fraction of galaxies that would be star-forming at low mass but are quenched at higher mass, at fixed environment. We also define a normalized difference between the two effects, to see which one is more dominant, as follows:

$$\Delta_{norm}(M_\star, z) = \frac{\epsilon_{env} - \epsilon_{mass}}{\epsilon_{env} + \epsilon_{mass}}. \tag{13}$$

The quenching efficiencies and the normalized difference between the two effects are presented in Figure 17. The earliest redshift bin showing nonzero values for both ϵ_{mass} and ϵ_{env} is $3.5 < z < 4.5$. However, due to the limited number of QGs at this epoch, it is not possible to determine which channel is dominant. At early times, quenching appears first at higher masses, and as galaxies evolve, at later times, quenched galaxies become more common at lower masses as well. This is consistent with the downsizing scenario, where galaxy quenching proceeds from high- to low-mass systems as the Universe evolves (L. L. Cowie et al. 1996; F. Fontanot et al. 2009). This trend may be partly influenced by sample limitations and selection effects, since detecting low-mass QGs at high redshift is challenging. At all redshifts, ϵ_{mass} increases with stellar mass, as expected if more massive galaxies are more strongly affected by mass-dependent quenching mechanisms. The first epoch in which mass quenching shows a dominant effect is $2.5 < z < 3.5$, where the mass efficiency exceeds environmental quenching effects. Environmental quenching efficiencies also rise with stellar mass, but generally with smaller amplitude. Comparing different epochs, both ϵ_{mass} and ϵ_{env} increase toward lower redshift, reflecting the growing impact of quenching over cosmic time. At high redshift, quenching is dominated by the mass channel, with environment playing only a minor role. For the normalized efficiencies, we show only bins with relative uncertainty ($\partial\Delta_{norm}/\Delta_{norm}$) less than 3. Above $z \sim 1.8$, mass quenching dominates across the full stellar-mass range. Even low-mass galaxies in this regime are more strongly affected by mass-related processes than by environmental factors. In the $0.8 < z < 1.2$ bin, the environmental quenching strength becomes comparable to the mass-quenching efficiency for low-mass galaxies, but mass quenching becomes dominant at higher masses. Below $z \sim 0.8$, however, the balance shifts. Environmental quenching becomes more effective than mass quenching at the low-mass end ($M_\star < 10^{10} M_\odot$), indicating that dense environments are increasingly capable of shutting down star formation in relatively small systems, through mechanisms such as ram pressure stripping or strangulation. With the increasing stellar mass in this low-redshift epoch, the efficiency of environmental quenching also rises, eventually reaching values comparable to mass quenching at the highest masses. By the present epoch, the most massive galaxies in dense regions appear to be shaped by a combination of both processes operating at similar strengths.

The balance between mass- and environment-driven quenching evolves with stellar mass and redshift, marking a transition in galaxy evolution pathways. At earlier times, internal processes tied to mass constitute the primary driver of star formation suppression in galaxy populations, even though mass has not been fully assembled. However, at later times, the environment exerts a stronger influence, making environmental quenching more dominant for low-mass systems and eventually matching the mass quenching in the most massive galaxies in the densest regions.

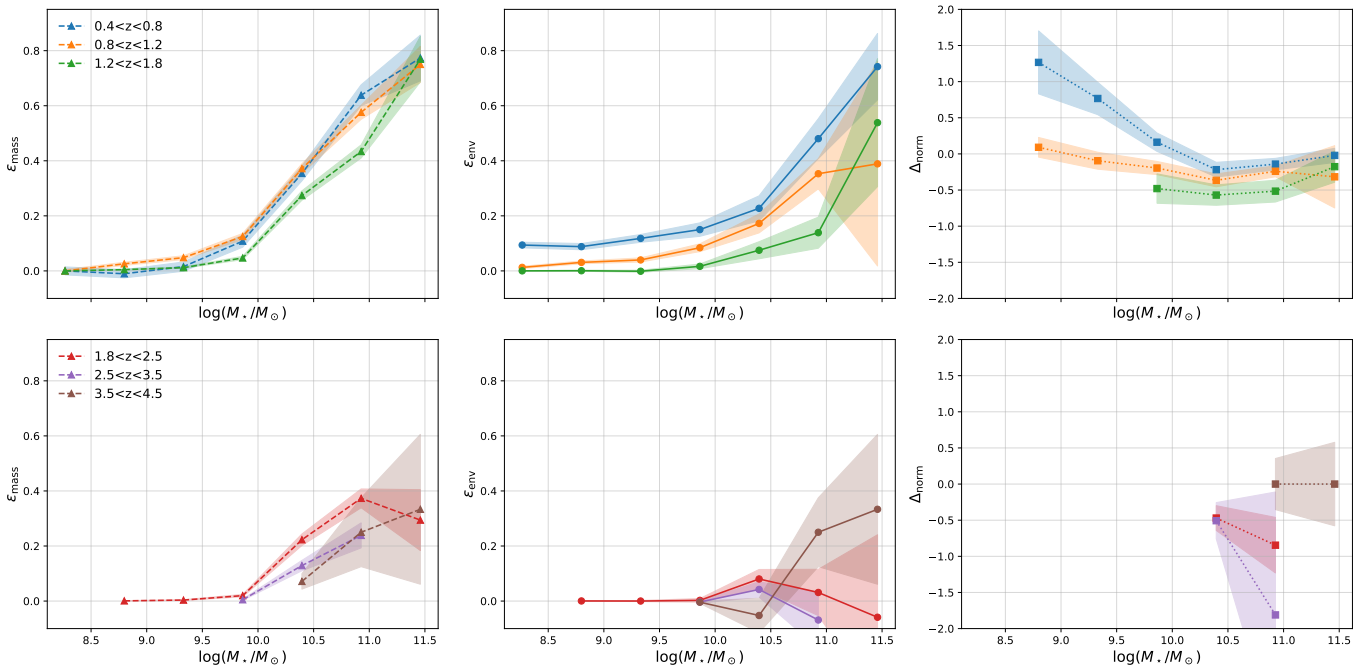

Figure 17. Quenching efficiencies as a function of stellar mass in different redshift bins. The top panels show redshift bins in the range $0.4 < z < 1.8$, and the bottom panels show $1.8 < z < 4.5$. The left panels show the environmental quenching efficiency, comparing the fraction of quenched galaxies in high- versus low-density environments. The middle panels present the mass-quenching efficiency, showing how quenching depends on stellar mass within dense regions. The right panels show the normalized strength, which quantifies whether quenching is primarily driven by environment (positive values) or by stellar mass (negative values). The shaded regions represent the uncertainties, which are binomial errors. For the normalized difference, the errors are propagated from mass and environment efficiencies, and only bins with relative uncertainty $(\partial\Delta_{\rm norm}/\Delta_{\rm norm}) < 3$ are shown. Mass quenching dominates at most redshifts and masses, while environmental quenching becomes stronger at $z < 0.8$ for low-mass galaxies.

Compared to previous work, our COSMOS-Web measurements push the study of quenching to higher redshifts and lower masses. For instance, the COSMOS2020 sample was very limited by its mass completeness, and for the redshift bin of $1.1 < z < 2$ COSMOS2020 is missing masses lower than $10^{9.5}M_{\odot}$, while for $2 < z < 4$ masses lower than $10^{10}M_{\odot}$ are missing (S. Taamoli et al. 2024b). This is also the case for the CANDELS field. Although the samples are not exactly comparable, the final outcome is mostly consistent. S. Taamoli et al. (2024b) reported that for COSMOS2020 at $2 < z < 4$, mass quenching dominates, while environmental quenching efficiencies become negative, meaning overdense regions enhance star formation, due to the abundant cold gas and frequent mergers. In contrast, we have already measured nonzero values for both quenching efficiencies at $z \sim 4$, although the limited statistics at these redshifts prevent a robust ranking between them. This suggests that environmental effects may set in earlier than inferred from COSMOS2020, but both studies agree that mass quenching remains the stronger process in general at higher redshifts. Similar conclusions were found by N. Chartab et al. (2020), who found that in the CANDELS field environmental quenching is negligible above $z \sim 1.5$ and mass quenching dominates across all stellar masses. Moving into intermediate redshifts ($1 \lesssim z \lesssim 2$), all studies converge on the continued dominance of mass quenching, with environmental effects still weak or marginal (N. Chartab et al. 2020; S. Taamoli et al. 2024b). In the ZFOURGE survey performed to $z \sim 2$, L. Kawinwanichakij et al. (2017) found that environmental and mass-quenching strengths are comparable for $M_{\star} > 10^{10.5}M_{\odot}$ at all redshifts. At lower redshifts ($z \lesssim 1$), however, we observe a rise in the environmental quenching efficiency at the low-mass end, which dominates the mass-quenching processes even for galaxies with $M_{\star} \lesssim 10^{10}M_{\odot}$. This is in line with the low-redshift behavior reported by Y.-j. Peng et al. (2010), L. Kawinwanichakij et al. (2017), N. Chartab et al. (2020), and S. Taamoli et al. (2024b), who all found that environmental quenching becomes increasingly important at late times, particularly for low-mass systems likely to be satellites in dense environments (Y.-j. Peng et al. 2012). Also, G. Toni et al. (2026) found that the QG fraction increases strongly with group richness below $z \sim 1$, highlighting the growing importance of dense environments in shutting down star formation at late times.

The observed interplay between mass, star formation, environment, and quenching shows a tightly connected, multidimensional framework of galaxy evolution. The mass–density relation (Figure 12) shows that, over time, galaxies in denser environments tend to build up more stellar mass, particularly in quiescent systems. At low redshifts, the suppression of star formation in dense environments leads to a higher abundance of quenched galaxies. In contrast, at higher redshifts, galaxies in overdense regions exhibit elevated SFRs, likely fueled by abundant cold gas. These environmental effects are reflected in the quenching efficiencies. At high redshift, mass quenching dominates across all environments, consistent with internal mechanisms regulating star formation as galaxies grow in mass. Toward lower redshifts, environmental quenching rises in importance, especially for low-mass systems. This shows the impact of dense surroundings on gas removal and accretion suppression. Taken together, our results suggest that the pathways by which galaxies grow and shut down star formation are fundamentally shaped by a combination of intrinsic properties (mass and gas content) and extrinsic

conditions (environment), with their relative importance evolving over cosmic time. This integrated view connects the physical processes driving the trends seen in stellar-mass buildup, star formation activity, and quenching, offering a comprehensive picture of how galaxies transition from star-forming to quiescent and evolve across environments and epochs.

6. Summary

We reconstruct the cosmic web density field in the COSMOS-Web field up to redshift of 9.5. Our selection criteria are summarized in Table 1. We choose a fixed comoving width of 35 h^{-1} Mpc for our slices, giving 157 slices in our sample. By assigning weights to each galaxy for each slice based on the redshift PDF, we generate density maps for each slice using the wKDE method, taking into account edge effects, adaptive bandwidths, and corrections for star-masked regions. This approach allows us to study the evolution of galaxies within different environments up to $z \sim 7$.

Compared to COSMOS2020, COSMOS-Web provides better mass completeness and improved, deeper photometric redshift precision. These advances lead to cleaner and more reliable reconstructions of LSS, with overdense regions no longer artificially inflated, underdense regions better preserved, and small-scale features more accurately recovered. COSMOS-Web also includes a larger number of faint, high-redshift galaxies, improving environmental statistics. While COSMOS2020 density maps were limited to about $z \sim 4$, COSMOS-Web allows us to extend the reconstruction reliably up to $z \sim 7$, offering a more accurate and deeper view of galaxy properties in environments.

We explore the relations between mass, SFR, sSFR, and quenching efficiencies with LSS densities at different epochs to see how environment shapes the characteristics of galaxies. Our results are summarized as follows:

1. The relation between stellar mass and environment shows that massive galaxies preferentially occupy overdense regions. This correlation is strongest at $z \lesssim 2.5$, particularly for QGs, while star-forming systems show a weaker dependence. At higher redshifts, the trend persists only in the most extreme overdensities, suggesting that the densest regions (e.g., protocluster environments) are the main sites of early mass assembly.
2. For the full population, SFR decreases with overdensity at $z \lesssim 1.2$, flattens at $1.2 < z < 1.8$, and reverses beyond $z \gtrsim 1.8$, where galaxies in dense regions show enhanced star formation. This overall trend is driven by QGs, which suppress the mean SFR in dense regions at low redshift ($z < 1.2$), while SFGs instead show a weak positive correlation with density up to $z \sim 5.5$. sSFR stays nearly flat for star-forming systems across all redshifts, but declines with density for QGs at $z \lesssim 1.2$ as SFR decreases and mass increases, consistent with environmental quenching. At higher redshift, the environmental dependence of both SFR and sSFR largely weakens, though overdense regions continue to host the most active SFGs.
3. Quenching efficiencies measured with COSMOS-Web show that both stellar mass and environment contribute to shutting down star formation, but their relative importance evolves with redshift. At high redshift ($z \gtrsim 2.5$), quenching is dominated by mass-related processes, with environment playing only a minor role. As redshift decreases, both efficiencies increase, and by $z < 0.8$ environmental quenching becomes stronger than mass quenching for low-mass galaxies ($M_\star \lesssim 10^{10} M_\odot$). In dense regions at low redshift, massive galaxies are governed by a combination of mass and environmental processes acting with comparable strength. These results indicate that internal mechanisms tied to mass dominate early quenching, while environmental effects grow at later times, especially for low-mass systems.

The observed correlations between stellar mass, star formation activity, quenching processes, and LSS density indicate that galaxy evolution has been shaped by both intrinsic and extrinsic factors across cosmic time. These observed links between galaxy properties and environment are made more reliable by the depth and precision of COSMOS-Web, which sets a new benchmark for LSS studies.

Acknowledgments

This work is based in part on observations made with the NASA/ESA/CSA James Webb Space Telescope. The data were obtained from the Mikulski Archive for Space Telescopes at the Space Telescope Science Institute, which is operated by the Association of Universities for Research in Astronomy, Inc., under NASA contract NAS 5-03127 for JWST. These observations are associated with program #1727 (COSMOS-Web). This project has received funding from the European Union's Horizon 2020 research and innovation program under the Marie Skłodowska-Curie grant agreement No 101148925. J.R.W. acknowledges that support for this work was provided by the Brinson Foundation through a Brinson Prize Fellowship grant.

Data Availability

The code developed for this work to construct the wKDE density maps is openly available on GitHub: hhatam/CosmicWeb. The repository includes all scripts used to generate the density maps, the density contrasts of galaxies, and for plotting each step of the method for redshift slices. The resulting catalog containing density maps and density contrasts of galaxies is publicly available. In addition, the repository contains a video that illustrates the evolution of LSSs across cosmic time. To further support outreach and interactive exploration, we have also released an augmented reality tool that enables users to visualize the COSMOS-Web density field in 3D. This tool is designed as an educational resource, allowing users to inspect how galaxies populate overdense and underdense regions in the cosmic web.

ORCID iDs

Hossein Hatamnia https://orcid.org/0009-0007-3673-4523
Bahram Mobasher https://orcid.org/0000-0001-5846-4404
Sina Taamoli https://orcid.org/0000-0003-0749-4667
Jeyhan S. Kartaltepe https://orcid.org/0000-0001-9187-3605
Caitlin M. Casey https://orcid.org/0000-0002-0930-6466
Hollis B. Akins https://orcid.org/0000-0003-3596-8794

Malte Brinch https://orcid.org/0000-0002-0245-6365
Nima Chartab https://orcid.org/0000-0003-3691-937X
Nicole E. Drakos https://orcid.org/0000-0003-4761-2197
Andreas L. Faisst https://orcid.org/0000-0002-9382-9832
Steven L. Finkelstein https://orcid.org/0000-0001-8519-1130
Maximilien Franco https://orcid.org/0000-0002-3560-8599
Finn Giddings https://orcid.org/0009-0003-2158-1246
Ghassem Gozaliasl https://orcid.org/0000-0002-0236-919X
Ali Hadi https://orcid.org/0009-0003-3097-6733
Aryana Haghjoo https://orcid.org/0009-0006-3071-7143
Santosh Harish https://orcid.org/0000-0003-0129-2079
Olivier Ilbert https://orcid.org/0000-0002-7303-4397
Pascale L. Jablonka https://orcid.org/0000-0002-9655-1063
Shuowen Jin https://orcid.org/0000-0002-8412-7951
Ali Ahmad Khostovan https://orcid.org/0000-0002-0101-336X
Anton M. Koekemoer https://orcid.org/0000-0002-6610-2048
Ronaldo Laishram https://orcid.org/0000-0002-0322-6131
Daizhong Liu https://orcid.org/0000-0001-9773-7479
Matteo Maturi https://orcid.org/0000-0002-3517-2422
Henry Joy McCracken https://orcid.org/0000-0002-9489-7765
Crystal L. Martin https://orcid.org/0000-0001-9189-7818
Lauro Moscardini https://orcid.org/0000-0002-3473-6716
Diana Scognamiglio https://orcid.org/0000-0001-8450-7885
Marko Shuntov https://orcid.org/0000-0002-7087-0701
Greta Toni https://orcid.org/0009-0005-3133-1157
Alexander de la Vega https://orcid.org/0000-0002-6219-5558
John R. Weaver https://orcid.org/0000-0003-1614-196X
Lilan Yang https://orcid.org/0000-0002-8434-880X

References

Abramson, I. S. 1982, AnSta, 10, 1217
Aihara, H., AlSayyad, Y., Ando, M., et al. 2022, PASJ, 74, 247
Ashby, M. L. N., Caputi, K. I., Cowley, W., et al. 2018, ApJS, 237, 39
Balogh, Michael, Eke, Vince, Miller, Chris, et al. 2004, MNRAS, 348, 1355
Baxter, D. C., Coil, A. L., Nadler, E. O., et al. 2025, ApJ, 990, 225
Behroozi, P. S., Wechsler, R. H., & Conroy, C. 2013, ApJ, 770, 57
Bekki, K. 1999, ApJL, 510, L15
Birnboim, Y., & Dekel, A. 2003, MNRAS, 345, 349
Bond, J. R., Kofman, L., & Pogosyan, D. 1996, Natur, 380, 603
Boselli, A., & Gavazzi, G. 2006, PASP, 118, 517
Brinch, M., Greve, T. R., Sanders, D. B., et al. 2024, MNRAS, 527, 6591
Brinch, M., Greve, T. R., Weaver, J. R., et al. 2023, ApJ, 943, 153
Bullock, J. S., & Boylan-Kolchin, M. 2017, ARA&A, 55, 343
Casey, C. M. 2016, ApJ, 824, 36
Casey, C. M., Akins, H. B., Shuntov, M., et al. 2024, ApJ, 965, 98
Casey, C. M., Kartaltepe, J. S., Drakos, N. E., et al. 2023, ApJ, 954, 31
Chabrier, G. 2003, PASP, 115, 763
Chartab, N., Mobasher, B., Darvish, B., et al. 2020, ApJ, 890, 7
Chartab, N., Newman, A. B., Rudie, G. C., et al. 2025, ApJ, 994, 106
Chiang, Y.-K., Overzier, R., & Gebhardt, K. 2013, ApJ, 779, 127
Colless, M., Peterson, B. A., Jackson, C., et al. 2003, arXiv:astro-ph/0306581
Coupon, J., Czakon, N., Bosch, J., et al. 2018, PASJ, 70, S7
Cowie, L. L., Songaila, A., Hu, E. M., & Cohen, J. G. 1996, AJ, 112, 839
Croton, D. J., Springel, V., White, S. D. M., et al. 2006, MNRAS, 365, 11
Daddi, E., Rich, R. M., Valentino, F., et al. 2022, ApJL, 926, L21
Darvish, B., Mobasher, B., Sobral, D., et al. 2016, ApJ, 825, 113
Darvish, B., Mobasher, B., Sobral, D., Scoville, N., & Aragon-Calvo, M. 2015, ApJ, 805, 121
Dekel, A., & Birnboim, Y. 2006, MNRAS, 368, 2
Dekel, A., Birnboim, Y., Engel, G., et al. 2009, Natur, 457, 451
Di Valentino, E., Mena, O., Pan, S., et al. 2021, CQGra, 38, 153001
Doroshkevich, A., Tucker, D. L., Allam, S., & Way, M. J. 2004, A&A, 418, 7
Elbaz, D., Daddi, E., Le Borgne, D., et al. 2007, A&A, 468, 33
Fabian, A. C. 2012, ARA&A, 50, 455
Fakhouri, O., Ma, C.-P., & Boylan-Kolchin, M. 2010, MNRAS, 406, 2267
Fontanot, F., De Lucia, G., Monaco, P., Somerville, R. S., & Santini, P. 2009, MNRAS, 397, 1776
Franco, M., Casey, C. M., Koekemoer, A. M., et al. 2026, ApJ, 999, 200
Gallazzi, A., Charlot, S., Brinchmann, J., White, S. D. M., & Tremonti, C. A. 2005, MNRAS, 362, 41
Genzel, R., Tacconi, L. J., Lutz, D., et al. 2015, ApJ, 800, 20
Ghaffari, Z., Gozaliasl, G., Biviano, A., et al. 2026, A&A, 708, A129
Giddings, F., Lemaux, B. C., Forrest, B., et al. 2026, A&A, 706, A55
Gozaliasl, G., Yang, L., Kartaltepe, J., et al. 2025, A&A, 703, A129
Grogin, N. A., Kocevski, D. D., Faber, S. M., et al. 2011, ApJS, 197, 35
Grützbauch, R., Conselice, C. J., Bauer, A. E., et al. 2011, MNRAS, 418, 938
Gunn, J. E., & Gott, J. R., III 1972, ApJ, 176, 1
Hall, P. 1982, Biometrika, 69, 383
Harish, S., Kartaltepe, J., Casey, C., Liu, D. & Cosmos-Web Team 2025, AAS Meeting, 245, 130.04
Hildebrandt, H., Viola, M., Heymans, C., et al. 2017, MNRAS, 465, 1454
Hopkins, P. F., Quataert, E., & Murray, N. 2012, MNRAS, 421, 3522
Ilbert, O., McCracken, H. J., Le Fèvre, O., et al. 2013, A&A, 556, A55
Jin, S., Sillassen, N. B., Magdis, G. E., et al. 2024, A&A, 683, L4
Jones, M. C. 1993, StCom, 3, 135
Joudaki, S., Blake, C., Johnson, A., et al. 2018, MNRAS, 474, 4894
Kauffmann, G., Heckman, T. M., White, S. D. M., et al. 2003, MNRAS, 341, 33
Kauffmann, G., White, S. D. M., Heckman, T. M., et al. 2004, MNRAS, 353, 713
Kawinwanichakij, L., Papovich, C., Quadri, R. F., et al. 2017, ApJ, 847, 134
Kennicutt, R. C., Jr. 1998, ARA&A, 36, 189
Kereš, D., Katz, N., Weinberg, D. H., & Davé, R. 2005, MNRAS, 363, 2
Khoshtinat, M., Hatamnia, H., & Baghram, S. 2024, MNRAS, 534, 1166
Koekemoer, A. M., Aussel, H., Calzetti, D., et al. 2007, ApJS, 172, 196
Koekemoer, A. M., Faber, S. M., Ferguson, H. C., et al. 2011, ApJS, 197, 36
Laigle, C., McCracken, H. J., Ilbert, O., et al. 2016, ApJS, 224, 24
Lemaux, B. C., Cucciati, O., Le Févre, O., et al. 2022, A&A, 662, A33
Lotz, J. M., Jonsson, P., Cox, T. J., et al. 2011, ApJ, 742, 103
Madau, P., & Dickinson, M. 2014, ARA&A, 52, 415
Maiolino, R., & Mannucci, F. 2019, A&ARv, 27, 3
Martig, M., Bournaud, F., Teyssier, R., & Dekel, A. 2009, ApJ, 707, 250
McCracken, H. J., Milvang-Jensen, B., Dunlop, J., et al. 2012, A&A, 544, A156
Mo, H. J., & White, S. D. M. 1996, MNRAS, 282, 347
Moore, B., Katz, N., Lake, G., Dressler, A., & Oemler, A. 1996, Natur, 379, 613
Moore, B., Lake, G., Quinn, T., & Stadel, J. 1999, MNRAS, 304, 465
Moster, B. P., Somerville, R. S., Maulbetsch, C., et al. 2010, ApJ, 710, 903
Muldrew, S. I., Hatch, N. A., & Cooke, E. A. 2015, MNRAS, 452, 2528
Muzzin, A., Marchesini, D., Stefanon, M., et al. 2013, ApJ, 777, 18
Naab, T., & Ostriker, J. P. 2017, ARA&A, 55, 59
Nelson, D., Pillepich, A., Springel, V., et al. 2018, MNRAS, 475, 624
Newman, A. B., Rudie, G. C., Blanc, G. A., et al. 2020, ApJ, 891, 147
Oke, J. B. 1974, ApJS, 27, 21
Overzier, R. A. 2016, A&ARv, 24, 14
Peng, Y., Maiolino, R., & Cochrane, R. 2015, Natur, 521, 192
Peng, Y.-j., Lilly, S. J., Kovač, K., et al. 2010, ApJ, 721, 193
Peng, Y.-j., Lilly, S. J., Renzini, A., & Carollo, M. 2012, ApJ, 757, 4
Perivolaropoulos, L., & Skara, F. 2022, NewAR, 95, 101659
Poggianti, B. M., Moretti, A., Gullieuszik, M., et al. 2017, ApJ, 844, 48
Pozzetti, L., Bolzonella, M., Zucca, E., et al. 2010, A&A, 523, A13
Rutkowski, M. J., Zabelle, B., Hagen, T., et al. 2025, ApJL, 983, L32
Sales, L. V., Wetzel, A., & Fattahi, A. 2022, NatAs, 6, 897
Sanders, D. B., Salvato, M., Aussel, H., et al. 2007, ApJS, 172, 86
Sawicki, M., Arnouts, S., Huang, J., et al. 2019, MNRAS, 489, 5202
Schawinski, K., Urry, C. M., Simmons, B. D., et al. 2014, MNRAS, 440, 889
Scognamiglio, D., Leroy, G., Harvey, D., et al. 2026, NatAs,
Scoville, N., Arnouts, S., Aussel, H., et al. 2013, ApJS, 206, 3
Scoville, N., Aussel, H., Brusa, M., et al. 2007, ApJS, 172, 1
Shen, S., Mo, H. J., White, S. D. M., et al. 2003, MNRAS, 343, 978
Shuntov, M., Akins, H. B., Paquereau, L., et al. 2025a, A&A, 704, A339
Shuntov, M., Ilbert, O., Toft, S., et al. 2025b, A&A, 695, A20
Snyder, G. F., Lotz, J. M., Rodriguez-Gomez, V., et al. 2017, MNRAS, 468, 207

Speagle, J. S., Steinhardt, C. L., Capak, P. L., & Silverman, J. D. 2014, ApJS, 214, 15
Springel, V., White, S. D. M., Jenkins, A., et al. 2005, Natur, 435, 629
Steidel, C. C., Adelberger, K. L., Dickinson, M., et al. 1998, ApJ, 492, 428
Sutherland, W., Emerson, J., Dalton, G., et al. 2015, A&A, 575, A25
Taamoli, S., Mobasher, B., Chartab, N., et al. 2024a, ApJ, 966, 18
Taamoli, S., Nezhad, N., Mobasher, B., et al. 2024b, ApJ, 977, 263
Tacconi, L. J., Genzel, R., Neri, R., et al. 2010, Natur, 463, 781
Tacconi, L. J., Genzel, R., & Sternberg, A. 2020, ARA&A, 58, 157
Taniguchi, Y., Kajisawa, M., Kobayashi, M. A. R., et al. 2015, PASJ, 67, 104
Taniguchi, Y., Scoville, N., Murayama, T., et al. 2007, ApJS, 172, 9
Tegmark, M., Blanton, M. R., Strauss, M. A., et al. 2004, ApJ, 606, 702
Terrazas, B. A., Bell, E. F., Pillepich, A., et al. 2020, MNRAS, 493, 1888
Toni, G., Gozaliasl, G., Maturi, M., et al. 2025, A&A, 697, A197
Toni, G., Maturi, M., Castignani, G., et al. 2026, A&A, 707, A87
Tremonti, C. A., Heckman, T. M., Kauffmann, G., et al. 2004, ApJ, 613, 898
van der Wel, A., Franx, M., van Dokkum, P. G., et al. 2014, ApJ, 788, 28
Ventou, E., Contini, T., Bouché, N., et al. 2019, A&A, 631, A87
Weaver, J. R., Kauffmann, O. B., Ilbert, O., et al. 2022, ApJS, 258, 11
Wetzel, A. R., Tinker, J. L., Conroy, C., & van den Bosch, F. C. 2013, MNRAS, 432, 336
White, S. D. M., & Rees, M. J. 1978, MNRAS, 183, 341
Wild, V., Almaini, O., Dunlop, J., et al. 2016, MNRAS, 463, 832
Woo, J., Dekel, A., Faber, S. M., et al. 2013, MNRAS, 428, 3306
Wright, G. S., Rieke, G. H., Glasse, A., et al. 2023, PASP, 135, 048003
Yang, L., Kartaltepe, J. S., Franco, M., et al. 2025, ApJS, 281, 68
York, D. G., Adelman, J., Anderson, J. E., Jr, et al. 2000, AJ, 120, 1579
Zel'dovich, Y. B. 1970, A&A, 5, 84